

# Nonlinear Reduced DNN Models for State Estimation\*

Wolfgang Dahmen <sup>†1</sup>, Min Wang <sup>‡2</sup>, and Zhu Wang <sup>§3</sup>

<sup>1,3</sup> Department of Mathematics, University of South Carolina, Columbia, SC 29208

<sup>2</sup> Department of Mathematics, Duke University, Durham, NC 27708

October 19, 2021

## Abstract

We propose in this paper a data driven state estimation scheme for generating nonlinear reduced models for parametric families of PDEs, directly providing *data-to-state maps*, represented in terms of Deep Neural Networks. A major constituent is a *sensor-induced* decomposition of a model-compliant Hilbert space warranting approximation in problem relevant metrics. It plays a similar role as in a Parametric Background Data Weak framework for state estimators based on Reduced Basis concepts. Extensive numerical tests shed light on several optimization strategies that are to improve robustness and performance of such estimators.

**Key Words:** State estimation in model-compliant norms, deep neural networks, sensor coordinates, reduced bases, ResNet structures, network expansion.

## 1 Introduction

Understanding complex “physical systems” solely through observational data is an attractive but unrealistic objective if one insists on certifiable accuracy quantification. This, in turn, is an essential precondition for prediction capability. In fact, unlike application scenarios where an abundance of data are available, data acquisition for “Physics Informed Learning Task” typically relies on sophisticated sensor technology and is often expensive or even harmful. Therefore, a central task is to develop efficient ways for fusing the information provided by data with *background information* provided by physical laws governing the observed states of interest, typically represented by partial differential equations (PDEs). In principle, this falls into the framework

---

\*This work was supported by National Science Foundation under grant DMS-2012469.

<sup>†</sup>E-mail: [dahmen@math.sc.edu](mailto:dahmen@math.sc.edu);

<sup>‡</sup>E-mail: [wangmin@math.duke.edu](mailto:wangmin@math.duke.edu);

<sup>§</sup>E-mail: [wangzhu@math.sc.edu](mailto:wangzhu@math.sc.edu);

of “Physics Informed Neural Networks” (PINN), however, with some noteworthy distinctions explained next.

The central objective of this note is to explore a machine learning approach to state estimation in the above sense. Our contributions concern two major aspects:

(i) In contrast to typical PINN formulations, we employ loss functions that are *equivalent* to the error of the estimator in a norm that is imposed by the continuous mathematical model. More precisely, this norm corresponds to a *stable variational formulation* of the PDE family. In other words, the generalization error for this loss function measures the accuracy of the estimator in a problem intrinsic norm without imposing any additional regularity properties.

(ii) When employing estimators, represented as Deep Neural Networks (DNNs), one has to accept a significant and unavoidable uncertainty about optimization success. Due to (i), one can at least measure the achieved accuracy at any stage of the optimization. We therefore take this fact as a starting point for a systematic *computational exploration* of a simple optimization strategy that seems to be particularly natural in combination with ResNet architectures.

Regarding (i), the proposed approach is, in principle, applicable to a much wider scope of problems than discussed below. Last but not least, in order to facilitate comparisons with other recovery schemes, specifically with methods that are based on *Reduced Basis* concepts, the numerical experiments focus on elliptic families of PDEs with *parameter dependent* diffusion fields. However, for this problem class we discuss in detail two rather different scenarios, namely diffusion coefficients with an *affine* parameter dependence, as well as *log-normal* parameter dependence. It is well known that the first scenario offers favorable conditions for Reduced Basis methods which have been well studied for this type of models and can therefore serve for comparisons. While in this case nonlinear schemes using neural networks do not seem to offer decisive advantages in terms of achievable certifiable estimation accuracy nor computational efficiency we see an advantage of the DNN approach in the second scenario because it seems that they can be better adapted to the challenges of this problem class.

It should be noted though that the present approach shares some conceptual constituents with so called One-Space methods or PBDW (Parametric Background Data Weak) methods (see [4, 2, 10]). We therefore briefly recollect some related basic ideas in Section 2.4. An important element is to represent the sensor functionals as elements of the trial space  $\mathbb{U}$  for the underlying PDE. The  $\mathbb{U}$ -orthogonal projection to their span, termed “measurement space”, provides a natural “zero-order approximation” to the observed state. To obtain an improved more accurate reconstruction, the data need to be “lifted” to the complement space. We view the construction of such a “lifting map” as “learning” the expected “label” associated with a given observation, see Section 2. This, in turn, is based on first projecting “synthetic data” in terms of parameter snapshots, to the  $\mathbb{U}$ -orthogonal complement of the measurement space. We then extract via SVD from these projected data a sufficiently accurate “effective” complement space that captures corresponding components of the solution manifold with high accuracy in  $\mathbb{U}$ . The lifting map is then expressed in terms of the coefficients of a  $\mathbb{U}$ -orthogonal basis of the effective complement space which, in turn,

are represented by a neural network. The fact that we learn the coefficients of a  $\mathbb{U}$ -orthogonal basis allows us to control the accuracy of the estimator in the problem-relevant norm. Thus, the proposed method is based on combining POD based model reduction with neural network regression. In this regard, it shares similar concepts with the recent work in [13] and [9]. However, a major distinction is that in [13, 9] the whole parameter-to-solution map is constructed while the present work focuses on generating directly a *data-to-state* map through regression in *sensor coordinates* (see Section 2.3).

Concerning (ii), successfully training a neural network remains a serious issue. Neither can one guarantee to actually exploit the expressive power of a given network architecture, nor does it seem possible to estimate the required computational cost. Therefore, it is more important to measure a given optimization outcome in a problem-relevant metric for making it possible to enable the assessment of the estimation quality obtained in the end. In the second part of the paper we computationally explore a natural training strategy that, as will show, renders optimization more reliable, stable and robust with regard to varying algorithmic parameters like depth, width or learning rates. To counter gradient decay when increasing depth, we opt for ResNet architectures. Moreover, we systematically compare standard stochastic gradient descent applied to all trainable parameters, termed “plain RNN training” to an *expansion strategy* that starts with a shallow network and successively adds further blocks in combination with a *blockwise optimization*. That is, at every stage we optimize only the trainables in a single block while freezing the remaining parameter budget. In that sense we do not fix any network architecture beforehand but expand it dynamically while monitoring loss-decay, see Subsection 3.2. Section 4 is then devoted to extensive numerical studies comparing plain RNN and the expansion strategy for both application scenarios.

## 2 Problem Formulation and Conceptual Preview

### 2.1 Parametric PDE models

For a wide scope of applications, the underlying governing laws can be represented by a family of partial differential equations (PDEs)

$$\mathcal{F}(u, \mathbf{y}; f) = 0, \quad \mathbf{y} \in \mathcal{Y}, \quad (2.1)$$

with data  $f$  and coefficients depending on parameters  $\mathbf{y}$  ranging over some compact parameter domain  $\mathcal{Y} \subset \mathbb{R}^{d_y}$ . Focusing on linear problems, what matters in the present context is to identify first a *stable variational formulation* for (2.1), i.e., to identify a(n infinite-dimensional) *trial-space*  $\mathbb{U}$  and a *test-space*  $\mathbb{V}$ , such that

$$\mathcal{F}(u, \mathbf{y}; f)(v) = 0 = f(v) - (\mathcal{B}_{\mathbf{y}}u)(v), \quad v \in \mathbb{V}, \quad (2.2)$$

is well-posed, meaning that the bilinear form

$$b(u, v; \mathbf{y}) = (\mathcal{B}_{\mathbf{y}}u)(v), \quad u \in \mathbb{U}, v \in \mathbb{V}, \quad (2.3)$$

satisfies the conditions of the Babuska-Necas Theorem (continuity-, inf-sup-, surjectivity-condition), [12].

When  $\mathbf{y}$  traverses  $\mathcal{Y}$  the respective solutions  $u(\mathbf{y})$  mark the viable states of interest and form what is often often called the *solution manifold*

$$\mathcal{M} := \{u(\mathbf{y}) : \mathcal{F}(u(\mathbf{y}), \mathbf{y}; f) = 0, \quad \mathbf{y} \in \mathcal{Y}\} \subset \mathbb{U}, \quad (2.4)$$

which is in most relevant cases a compact subset of  $\mathbb{U}$ . The central task considered in this work is to recover, from a moderate number of measurements, a state  $u \in \mathbb{U}$  under the prior  $u \in \mathcal{M}$ .

Stable formulations are available for a wide scope of problems to which the following approach then applies. To be specific, we focus as a guding example second order elliptic problems

$$\mathcal{F}(u, \mathbf{y}; f) = f - \mathcal{B}_{\mathbf{y}}u := f + \operatorname{div}(a(\cdot; \mathbf{y})\nabla u), \quad \text{in } \Omega \subset \mathbb{R}^{d_x}, \quad u|_{\partial\Omega} = 0, \quad (2.5)$$

where  $f$  is a forcing term. Examples are Darcy's equation for the pressure in ground-water flow or electron impedance tomography. Both involve second order elliptic equations as core models and *parameter dependent* diffusion coefficients that describe permeability or conductivity, respectively, where in the latter case the model is complemented by Robin-type boundary conditions. A large parameter dimension  $d_y$  reflects substantial model complexity. In a probabilistic framework, the parametric representations of the coefficients could arise, for instance, from Karhunen-Loëve expansions of a random field that represent numerically "unresolvable" features. In this case the number of parameters is ideally *infinite* and parameter truncation causes additional model bias.

For (2.5) a proper choice of trial- and test-spaces is  $\mathbb{U} = \mathbb{V} = H_0^1(\Omega)$ , provided that one has *uniform ellipticity*, namely there exist constants  $0 < r \leq R < \infty$  such that

$$r \leq a(\cdot, \mathbf{y}) \leq R, \quad \text{in } \Omega, \quad \mathbf{y} \in \mathcal{Y}. \quad (2.6)$$

For other problem types, such as convection dominated problems or time-space formulations for parabolic problems, one may have to choose  $\mathbb{V}$  differently from  $\mathbb{U}$ , see e.g. [7, 8].

Later in our numerical examples we consider two types of diffusion coefficients:

(S1) *Piecewise constant coefficients:* Given  $\{\Omega_j\}_{j \in I}$  a non-overlapping partition of  $\Omega$ ,  $\bigcup_{j \in I} \Omega_j = \Omega$ , the diffusion coefficient in the model (2.5) is assumed to be of the following form:

$$a(x; \mathbf{y}) = a_0(x) + \sum_{j \in I} y_j \chi_j(x), \quad (2.7)$$

where  $y_j$ , the  $j$ -th component of  $\mathbf{y}$ , obeys a uniform distribution and  $\chi_j(x)$  is the characteristic function that takes the values 1 in  $\Omega_j$  and 0 in its complement  $\Omega \setminus \Omega_j$ . This correponds to the affine parameter representation (2.7). We assume for simplicity  $a_0(x) = 1$  and  $y_j \sim U[-1/2, 1/2]$  so that the diffusion coefficient is piecewise constant while the uniform ellipticity (2.6) of the problem is guaranteed with a moderate condition of the variational formulation.

(S2) *Lognormal case:* Suppose the diffusion coefficient has the following parameterized form:

$$a(x; \mathbf{y}) = a_0(x) + a_1 e^{z(x, \mathbf{y})}, \quad (2.8)$$

where  $a_0$  is a continuous non-negative function on  $\overline{\Omega}$ ,  $a_1$  is a positive constant and  $z(x, \mathbf{y})$  is a zero-mean Gaussian random field

$$z(x, \mathbf{y}) = \sum_{j=1}^{\infty} \sqrt{\mu_j} \xi_j(x) \eta_j(\mathbf{y}), \quad x \in \Omega \text{ and } \mathbf{y} \in \mathcal{Y}.$$

Here,  $\{\eta_j\}_{j \geq 1}$  form an orthogonal system over  $\mathcal{Y}$  where the components of  $\mathbf{y}$  are i.i.d.  $\mathcal{N}(0, 1)$ , and the sequence  $\{(\mu_j, \xi_j)\}_{j \geq 1}$  are real eigenpairs of the covariance integral operator

$$(Cv)(x) = \int_D c(x, x') v(x') dx'$$

associated with the Matérn model

$$c(x, x') = \sigma^2 \frac{2^{1-\nu}}{\Gamma(\nu)} (2\sqrt{\nu} r)^\nu K_\nu(2\sqrt{\nu} r),$$

in which  $\sigma^2$  is the marginal variance,  $\nu > \frac{1}{2}$  is the smoothness parameter of the random field,  $\Gamma$  is the Gamma function,  $r = \sqrt{\frac{(x_1 - x'_1)^2}{\lambda_{x_1}^2} + \frac{(x_2 - x'_2)^2}{\lambda_{x_2}^2}}$ ,  $\lambda_{x_1}$  and  $\lambda_{x_2}$  are the correlation lengths along  $x_1$ - and  $x_2$ -coordinates, and  $K_\nu$  the modified Bessel function of second kind.

At the discrete level, to generate realizations of the stationary Gaussian process over the grid points of  $\Omega$ , we use the circulant embedding approach in [15, 14]. Its main idea is to embed the covariance matrix to a block circulant matrix so that FFT can be applied for a fast evaluation.

The reason for considering these two scenarios lies in the following principal distinctions: In scenario (S1) the choice of  $\mathcal{Y}$  ensures that the diffusion parameter always satisfies (2.6) so that

$$a(u, v; \mathbf{y}) := \int_{\Omega} a(\cdot; \mathbf{y}) \nabla u \cdot \nabla v \, dx = f(v), \quad v \in \mathbb{U}. \quad (2.9)$$

is stable over  $\mathbb{U} = H_0^1(\Omega) = \mathbb{V}$  and possesses for each  $\mathbf{y} \in \mathcal{Y}$  a unique weak solution  $u = u(\mathbf{y}) \in \mathbb{U}$ . However, the condition of (2.9) depends on  $R/r$  and deteriorates when this quotient grows. In scenario (S2) this latter aspect is aggravated further because (2.6) holds only with high probability. Moreover, in contrast to scenario (S1), the diffusion coefficient no longer is affine in  $\mathbf{y} \in \mathcal{Y}$  which is known to poses challenges to the construction of certifiable Reduced Bases, see e.g. [11].

## 2.2 Sensors and Data

In addition to the model assumption that an observed state  $u \in \mathbb{U}$  (nearly-) belongs to  $\mathcal{M}$  we wish to utilize external information in terms of measurements or data. Throughout this note we

will assume that the number  $m$  of measurements  $\mathbf{o} = (o_1, \dots, o_m)^\top \in \mathbb{R}^m$  of an unknown state  $u$  is fixed and of moderate size. We will always assume that the data are produced by *sensors*

$$o_i = \ell_i(u), \quad i = 1, \dots, m, \quad \boldsymbol{\ell} := (\ell_1, \dots, \ell_m) \in (\mathbb{U}')^m, \quad (2.10)$$

i.e., we assume, for simplicity, in what follows the  $\ell_i$  to be *bounded linear functionals*.

Estimating  $u$  from such data is ill-posed, already due to a possible severe under-sampling. Under the assumption that  $u$  (at least nearly) satisfies the PDE for *some* parameter  $\mathbf{y} \in \mathcal{Y}$  one may also ask for such a parameter  $\mathbf{y}$  that explains the data best. Since the *parameter-to-solution map*  $\mathbf{y} \rightarrow u(\mathbf{y})$  is not necessarily injective, this latter parameter estimation problem is typically even more severely ill-posed and nonlinear.

A common approach to regularizing both estimation tasks is *Bayesian inversion*. An alternative is to fix from the start a presumably good enough discretization, say in terms of a large finite element space  $\mathbb{U}_h$  to then solve (a large scale optimization) problem

$$\min_{\mathbf{y} \in \mathcal{Y}, u_h \in \mathbb{U}_h} \left\{ \|\mathbf{o} - \boldsymbol{\ell}(u_h)\|^2 + \lambda \|\mathcal{F}_h(u_h, \mathbf{y}; f)\|^2 + \mu \|R_h(u_h)\|^2 \right\}, \quad (2.11)$$

where  $\|\cdot\|$  is just the Euclidean norm,  $\lambda$  and  $\mu$  are weight parameters and the last summand represents a regularization term which is needed since  $d_y + \dim \mathbb{U}_h$  is typically much larger than the number of measurements  $m$ . Questions arising in this context are: How to choose  $\lambda, \mu$  and the regularization operator  $R_h$ ; perhaps, more importantly, should one measure deviation from measurements and the discrete residual - closeness to the model - in the *same* metric?

Moreover, for each new data instance  $\mathbf{o}'$  one has to solve the same large-scale problem again. Thus, employing a *reduced model* for approximating the *parameter-to-solution map*  $\mathbf{y} \mapsto u(\mathbf{y})$  would serve two purposes, namely mitigating under-sampling and speeding forward simulations. Specifically, we apply similar concepts as in [2, 10, 4, 6] to base state estimation on *reduced modeling*, as described next.

### 2.3 Sensor-Coordinates

Rather than tying a discretization directly to the estimation task, and hence to a specific regularization, as in (2.11), reduced order modeling methods such as the Reduced Basis Methods (RBM) first prepare in an *offline phase* a reduced order model that requires the bulk of computation. It typically takes place in a “truth-space”  $\mathbb{U}_h \subset \mathbb{U}$ , usually a finite element space of sufficiently large dimension that is expected to comply with envisaged estimation objectives (which could be even adjusted at a later stage). In particular, the reduced order model can be adapted to the solution manifold and the sensor system. As such it is only used indirectly in the recovery process and should be viewed as representing “computing in  $\mathbb{U}$ ”. A first important ingredient of the methods in [2, 10, 4, 6] is to *Riesz-lift* the functionals in  $\boldsymbol{\ell}$  from  $\mathbb{U}'$  to  $\mathbb{U}$ , thereby subjecting them to the same metric as the states  $u$ . The obtained Riesz-representers  $\phi_i \in \mathbb{U}$  of  $\ell_i \in \mathbb{U}'$  then span an  $m$ -dimensional subspace  $\mathbb{W} \subset \mathbb{U}$ , referred to as *mesurement space*. Thus,  $\mathbb{U}$ -orthogonal

projections  $P_{\mathbb{W}}u$  of some  $u \in \mathbb{U}$  to  $\mathbb{W}$  encode the same data-information about  $u$  as  $\mathbf{o} = \ell(u)$ . This induces the decomposition

$$\mathbb{U} = \mathbb{W} \bigoplus \mathbb{W}^\perp, \quad u = P_{\mathbb{W}}u + P_{\mathbb{W}^\perp}u, \quad (2.12)$$

so to speak representing any state  $u$  in ‘‘sensor coordinates’’  $w = P_{\mathbb{W}}u$ , and ‘‘labels’’  $w^\perp = P_{\mathbb{W}^\perp}u$ .

In these terms, recovering a state  $u$  from its measurement  $w = P_{\mathbb{W}}u$ , means to approximate the label  $P_{\mathbb{W}^\perp}u \in \mathbb{W}^\perp$ . Thus, the state estimation can be viewed as seeking a map

$$A : w \mapsto A(w), \quad A(w) = w + B(w), \quad (2.13)$$

where, in principle,  $B : \mathbb{W} \rightarrow \mathbb{W}^\perp$  could be any map that hopefully exploits the fact that  $w = P_{\mathbb{W}}u$  for some  $u \in \mathcal{M}$  in an effective way.

## 2.4 Affine Recovery Map

The methods in [2, 10, 4] determine the *lifting-map*  $B : \mathbb{W} \rightarrow \mathbb{W}^\perp$  as a *linear* or *affine* map, termed as ‘‘One-Space-Methods’’, and in [6] as a *piecewise affine* map combining One-Space concepts with parameter domain decomposition and model selection. As shown in [4], any affine map  $B$  is characterized by an *affine* subspace  $\mathbb{U}_n = \bar{u} + \tilde{\mathbb{U}}_n \subset \mathbb{U}$ , where  $\bar{u}$  is a suitable chosen offset state and  $\tilde{\mathbb{U}}_n$  is a linear space of dimension  $n$ , for which the estimator  $A = A_{\mathbb{U}_n}$  satisfies

$$u^*(w) := A_{\mathbb{U}_n}(w) = \operatorname{argmin}\{u \in w + \mathbb{W}^\perp : \|u - P_{\mathbb{U}_n}u\|_{\mathbb{U}}\}. \quad (2.14)$$

Moreover,  $u^*(w)$  can be computed efficiently as a linear least-squares problem in  $\mathbb{U}_n$  followed by a simple correction in  $\mathbb{W}$ . Uniqueness is ensured if

$$\mu(\tilde{\mathbb{U}}_n, \mathbb{W}) := \sup_{v \in \mathbb{U}_n} \frac{\|v\|_{\mathbb{U}}}{\|P_{\mathbb{W}}v\|_{\mathbb{U}}} < \infty, \quad (2.15)$$

which is the case if and only if  $\mathbb{U}_n \cap \mathbb{W}^\perp = \{0\}$ .  $\mu(\tilde{\mathbb{U}}_n, \mathbb{W})$  is actually computable as one over the smallest singular value of the cross-Gramian of an basis for  $\mathbb{U}_n$  and  $\mathbb{W}$ . Hence, it has a geometric interpretation because it relates to the *angle* between the spaces  $\tilde{\mathbb{U}}_n$  and  $\mathbb{W}$ , tending to infinity when this angle approaches  $\pi/2$ . This affects estimation accuracy directly since

$$\sup_{u \in \mathcal{M}} \|u^*(P_{\mathbb{U}_n}u) - u\|_{\mathbb{U}} \leq \mu(\tilde{\mathbb{U}}_n, \mathbb{W})\varepsilon_n, \quad \text{when } \operatorname{dist}(\mathcal{M}, \mathbb{U}_n)_{\mathbb{U}} := \sup_{u \in \mathcal{M}} \inf_{z \in \mathbb{U}_n} \|u - z\|_{\mathbb{U}} \leq \varepsilon_n. \quad (2.16)$$

This is actually best possible when using, as sole prior, the knowledge that  $u \in \mathcal{M}$  also belongs to the convex set  $\mathcal{K}(\mathbb{U}_n, \varepsilon_n) := \{u \in \mathbb{U} : \inf_{z \in \mathbb{U}_n} \|u - z\|_{\mathbb{U}} \leq \varepsilon_n\}$ , [2]. Thus, overall estimation accuracy involves a competition between the approximation property of the space  $\mathbb{U}_n$  and ‘‘visibility’’ from  $\mathbb{W}$ . In fact,  $\mathbb{U}_n$  can have at most dimension  $n = m$  since otherwise  $\mu(\tilde{\mathbb{U}}_n, \mathbb{W}) = \infty$ . Hence, the rigidity of an affine space severely limits estimation quality. In fact, it is shown in [6] that restricting to such convex priors will generally fail to meet natural estimation benchmarks which calls for employing *nonlinear reduced models*.

In this regard, the following comments will provide some orientation. One-space-methods appear to nevertheless perform very well for problems where the solution manifold  $\mathcal{M}$  has rapidly decaying Kolmogorov  $n$ -widths

$$d_n(\mathcal{M})_{\mathbb{U}} := \inf_{\dim \mathbb{V}_n \leq n} \text{dist}(\mathcal{M}, \mathbb{V}_n)_{\mathbb{U}}. \quad (2.17)$$

For elliptic problems (2.5) this is known to be the case, even in high parameter dimensional regimes, when (2.6) holds and the diffusion coefficients depend *affinely* on the parameters, as is the case in scenario (S1), (2.7). Approximations from judiciously chosen linear spaces can then be very effective. Moreover, affine parameter-dependence is also instrumental in the *greedy* construction methods of Reduced Bases for rate-optimal reduced linear models which play a central role in one-space-methods, [11, 1, 7, 5, 6]. It is therefore interesting to see how the nonlinear estimators proposed in the present paper compare with affine recovery methods in scenarios where the latter are known to perform well. For this reason we include scenario (S1) in our numerical tests.

That said, the effectivity of one-space-methods depends in a rather sensitive way on the above favorable conditions, namely rapid decay of  $n$ -widths, uniform ellipticity, and affine parameter dependence. We therefore include scenario (S2) with log-normal parameter dependence. In fact, affine dependence no longer holds, the behavior of  $n$ -widths is much less clear, and the coefficient field may nearly degenerate, challenging the validity of (2.6).

## 2.5 A Regression Framework

To avoid monitoring pointwise errors in high-dimensions we opt now for a mean-square accuracy quantification which responds in a less sensitive way to high parameter dimensionality and blends naturally into a learning context. A natural probabilistic model could be based on a probability measure  $\mu$  on  $\mathbb{U}$  with support on  $\mathcal{M}$ .  $u = (w = P_{\mathbb{W}}u, w^\perp = P_{\mathbb{W}^\perp}u)$ , is then viewed as a random variable. The optimal estimator would then be the nonlinear map

$$A^*(w) = w + B^*(w), \quad (2.18)$$

where the conditional expectation  $B^*(w) = \int_{w+\mathbb{W}^\perp} P_{\mathbb{W}^\perp} u d\mu(u|w)$  is the *regression function* minimizing

$$\int_{\mathbb{U}} \|u - A(P_{\mathbb{W}}u)\|_{\mathbb{U}}^2 d\mu(u) = \int_{\mathbb{W}} \int_{w+\mathbb{W}^\perp} \|w^\perp - B(w)\|_{\mathbb{U}}^2 d\mu(u|w) d\mu(w) \quad (2.19)$$

over all mappings of the form  $A(w) = w + B(w)$ ,  $B : \mathbb{W} \rightarrow \mathbb{W}^\perp$ .

The central goal in what follows is to construct numerical estimators that approximate  $B^*$  well. Note that this approximation should take place in  $\mathbb{U}$  for the estimator to respect the natural problem metrics.

### 3 State Estimation Algorithm

#### 3.1 Computational Setting

We describe next in more details how to set up a learning problem in the problem compliant norm  $\|\cdot\|_{\mathbb{U}}$ . We adhere to the sensor-induced decomposition (2.12). Of course, the underlying Riesz-lifts of the measurement functionals  $\ell$  cannot be computed exactly but need to be approximated within controllable accuracy. In the spirit of Reduced Basis methodology, we employ a sufficiently large “truth space”  $\mathbb{U}_h \subset \mathbb{U}$ , which we choose here as a conforming finite element space. The scheme is based on the following steps.

**(1) The Measurement Space:** As a major part of the offline stage, one then solves the  $m$  Galerkin problems

$$(\tilde{\phi}_h^i, v_h)_{\mathbb{U}} = \ell_i(v_h), \quad \forall v_h \in \mathbb{U}_h, \text{ and } i = 1, \dots, m, \quad (3.20)$$

providing (approximate) *Riesz representers*  $\tilde{\phi}_h^i \in \mathbb{U}_h$  of the linear functionals  $\ell_i$ . Then define

$$\mathbb{W}_h := \text{span}\{\phi_h^1, \dots, \phi_h^m\} \quad (3.21)$$

where the  $\{\phi_h^1, \dots, \phi_h^m\}$  result from orthonormalizing the lifted functionals  $\{\tilde{\phi}_h^1, \dots, \tilde{\phi}_h^m\}$ . Hence,

$$P_{\mathbb{W}_h} u := \sum_{i=1}^m (u, \phi_h^i)_{\mathbb{U}} \phi_h^i, \quad (3.22)$$

is the orthogonal projector from  $\mathbb{U}_h$  onto  $\mathbb{W}_h$  that encodes the information provided by the sensor system as elements of the trial space  $\mathbb{U}_h$ .

Specifically, given an observation vector  $\ell(u) \in \mathbb{R}^m$  of some observed state  $u \in \mathbb{U}$ , we can determine  $P_{\mathbb{W}_h}(u)$  as follows. Let  $\tilde{\Phi}, \Phi \in \mathbb{U}_h^m$  denote the column vectors, obtained by lining up the functions  $\tilde{\phi}_h^i, \phi_h^i$ ,  $i = 1, \dots, m$ . Moreover let  $\mathbf{C} \in \mathbb{R}^{m \times m}$  denote the (lower triangular) matrix that realizes the change of bases  $\mathbf{C}\tilde{\Phi} = \Phi$ . One readily checks that

$$\mathbf{w} := \mathbf{C}\ell(u_h) = ((u_h, \phi_h^1)_{\mathbb{U}}, \dots, (u_h, \phi_h^m)_{\mathbb{U}})^\top, \quad (3.23)$$

i.e., the  $\mathbb{U}$ -orthogonal projection of  $u$  to the measurement space  $\mathbb{W}_h$  is given by

$$P_{\mathbb{W}_h} u = \sum_{i=1}^m w_i \phi_h^i =: \Phi^\top \mathbf{w}, \quad (3.24)$$

providing the best approximation to an observed space from  $\mathbb{W}_h$ . This can therefore be viewed already as a “zero-order” reconstruction of the observed space in  $\mathbb{W}_h \subset \mathbb{U}$ .

Note that the problems (3.20) are always *elliptic* Galerkin problems, regardless of the nature of (2.1). The Riesz-lift (as a mapping from  $\mathbb{U}'$  to  $\mathbb{U}$ ) has condition number equal to one. Therefore, these preparatory offline calculations are stable and often a posteriori error estimates allow one assess the accuracy of Riesz-lifts, controlled by the choice of the truth space  $\mathbb{U}_h \subset \mathbb{U}$ . This should

not be confused with the accuracy of  $P_{\mathbb{W}_h}u$  with respect to  $u$  which is primarily limited by the number and type of sensors.

So far, we have ignored noise of the data  $\mathbf{o} = \ell(u)$ . Noise in the observation vector  $\mathbf{o}$  carries over to noise in the coefficients  $\mathbf{w}$  from (3.23) possibly inflated by the condition of the transformation matrix  $\mathbf{C}$ , see [6] for a more detailed discussion of this issue.

Our subsequent numerical experiments refer to the model problem (2.5) where the sensors are given by the local averages of  $u$  over subdomains  $B_i \subset \Omega$

$$\ell_i(u(x, \mathbf{y})) = \frac{1}{|B_i|} \int_{B_i} u(x, \mathbf{y}) dx, \quad (3.25)$$

with local neighborhoods  $B_i$ , and where the diffusion coefficients are piecewise constants on a  $4 \times 4$  checkerboard partition of  $\Omega$ , see (2.7). Thus the parametric dimension is 16.

Specifically, in subsequent experiments we realize those by taking the average value of the FE solutions at the four points of a small square  $B_i$  enclosing the sensor location. Denoting these four points by  $\{x_{p_j}\}_{j=1}^4$ , we have

$$\ell_i(u_h(\mathbf{y})) = \frac{1}{4} \sum_{j=1}^4 u_h(x_{p_j}, \mathbf{y}), \quad (3.26)$$

entering the right hand side of (3.20). A numerical illustration of selected normalized basis,  $\phi_h^1, \phi_h^6, \phi_h^{11}, \phi_h^{16}$ , is given in Figure 1, where the normalized basis vectors are obtained by the SVD of the matrix formed by the finite element coefficient vectors of the lifted functionals with respect to the inner product weighted by  $(v_h, v_h)_{\mathbb{U}}$ .

**(2) Generating Synthetic Data:** We randomly pick a set of parameter samples  $\mathbf{y}^s$ , for  $s = 1, \dots, \hat{N}$ , and employ a standard solver to compute the FE solutions  $u_h^s = u_h(x; \mathbf{y}^s) \in \mathbb{U}_h$  as “snapshots” at the selected parameter values. These FE solutions provide the high-fidelity “truth” data to be later used for training the estimator towards minimizing the regression objective (2.19). Corresponding synthetic measurements then take the form

$$\mathbf{w}^j = (w_{h,1}^j, \dots, w_{h,m}^j)^\top, \quad w_h^j := P_{\mathbb{W}_h} u_h^j = \sum_{i=1}^m w_{h,i}^j \phi_h^i, \quad j = 1, \dots, \hat{N}. \quad (3.27)$$

as detailed by (3.23) and (3.24).

In addition we need the “training labels” providing complement information

$$z_h^s = (I - P_{\mathbb{W}_h}) u_h^s, \quad s = 1, \dots, \hat{N}. \quad (3.28)$$

**(3) Approximate  $\mathbb{W}_h^\perp$ :** To extract the essential information provided by  $z_h^s$ , we perform next a singular value decomposition to the resulting point-cloud of finite-element coefficient vectors  $\mathbf{z}_h^s \in \mathbb{R}^{N_h}$ . Suppose we envisage an overall estimation target tolerance  $\eta > 0$ . We then retain only those  $k$  left singular vectors corresponding to singular values larger than or equal to a value  $\tilde{\eta}$

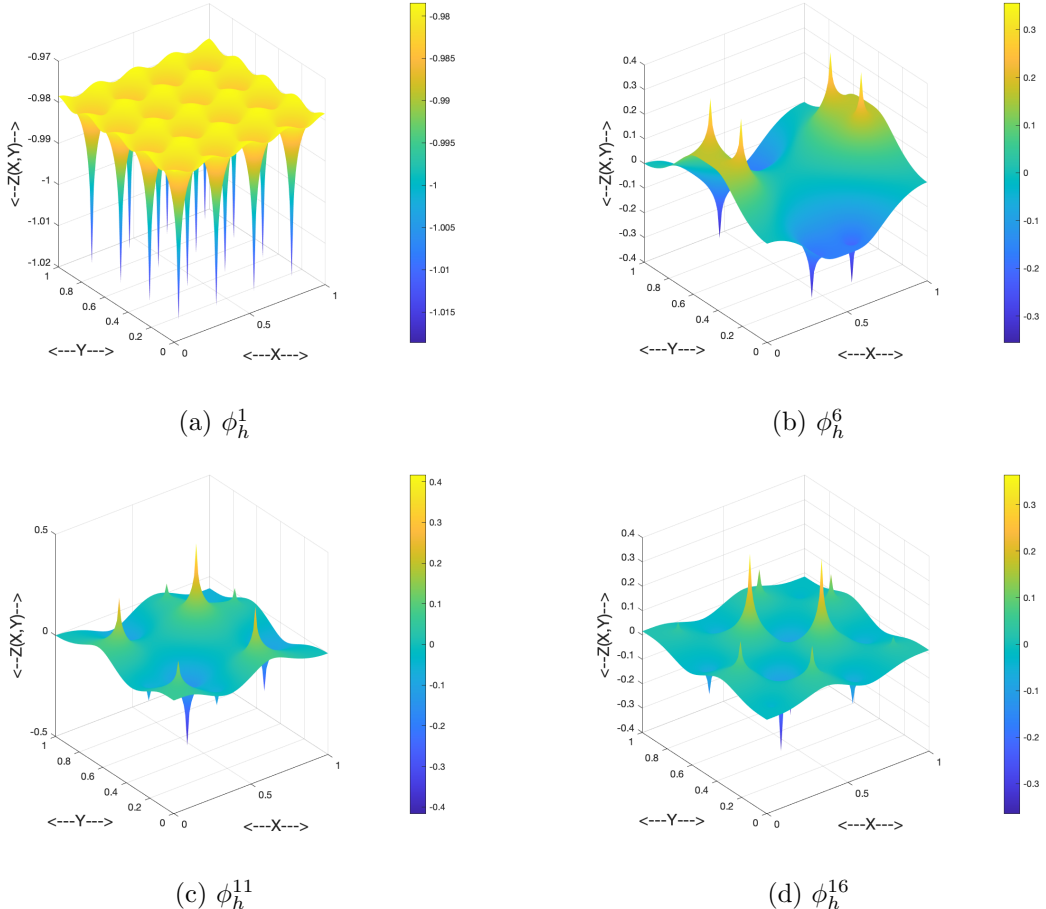


Figure 1: Example basis functions of the measurement space  $\mathbb{W}_h$ .

which is typically less than  $\eta$ , for the following reason. First, incidentally, the SVD and the decay of singular values indicate whether the complement information of  $\mathcal{M}$  can be adequately captured by a linear space of acceptable size within some target tolerance. While the  $H^1$ -norms of the  $z_h^s$  are uniformly bounded, the coefficients  $\mathbf{z}_h^s$  in their respective finite element representation convey accuracy only in  $L_2$ , and so does the truncation of singular values. Strictly speaking, employing standard inverse inequalities, one should take  $\tilde{\eta} \leq h\eta$ , where  $h$  is the mesh-size in  $\mathbb{U}_h$ .

We next  $\mathbb{U}$ -orthonormalize the finite element functions corresponding to the retained left singular vectors, arriving at a  $\mathbb{U}$ -orthonormal basis  $\Psi = \{\psi_h^1, \dots, \psi_h^k\} \subset \mathbb{W}_h^\perp$ . We then define

$$\widetilde{\mathbb{W}}_h^\perp := \text{span}\{\psi_h^1, \dots, \psi_h^k\} \quad (3.29)$$

as our *effective complement space* that accommodates the training labels  $c_h^s$  given by

$$c_h^s(x) := P_{\mathbb{W}_h^\perp} u_h^s = \sum_{i=1}^k c_i^s \psi_h^i = \Psi^\top \mathbf{c}^s, \quad c_i^s := (u_h^s, \psi_h^s)_{\mathbb{U}}, \quad s = 1, \dots, \hat{N}. \quad (3.30)$$

Note that  $c_h^s$  is essentially a compression of  $z_h^s$ .

In brief, after projecting the snapshot data into the complement of the measurement space, we determine a set of orthogonal basis  $\psi_h^j$  that optimally approximates the data in the sense that

$$\min_{\{\psi_h^1, \dots, \psi_h^k\}} \frac{1}{\widehat{N}} \sum_{s=1}^{\widehat{N}} \left\| z_h^s - \sum_{j=1}^k (z_h^s, \psi_h^j)_{\mathbb{U}} \psi_h^j \right\|_{\mathbb{U}}^2$$

subject to the conditions  $(\psi_h^j, \psi_h^i)_{\mathbb{U}} = \delta_{i,j}$ ,  $1 \leq i, j \leq k$ , where  $\delta_{i,j}$  is the Kronecker delta function. A numerical illustration of the normalized basis of  $\widetilde{\mathbb{W}}_h^\perp$ ,  $\psi_h^1, \psi_h^6, \psi_h^{11}, \psi_h^{16}$ , is shown in Figure 2.

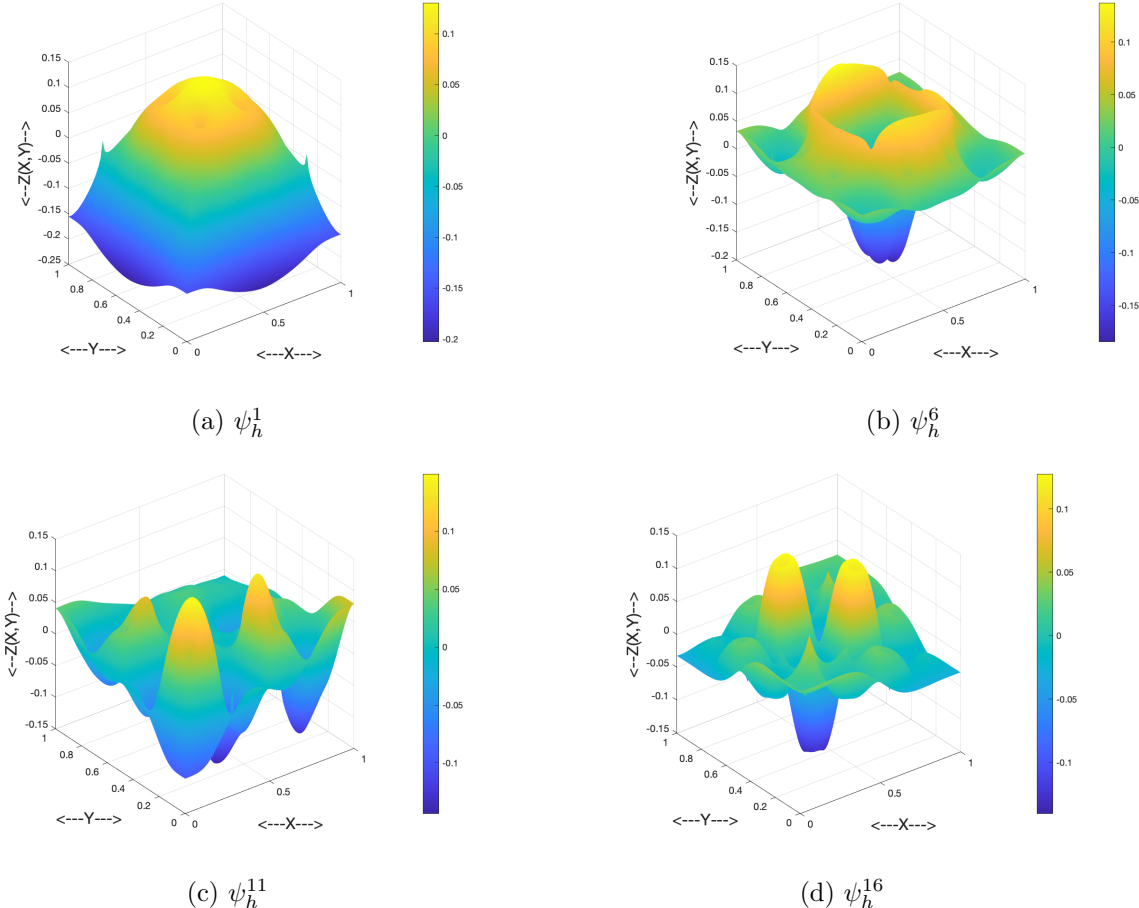


Figure 2: Example basis functions of the complement space  $\widetilde{\mathbb{W}}_h^\perp$ .

### Remark 1

Approximation in  $\mathbb{U}$  is now realized by training coefficient vectors in the Euclidean norm of  $\mathbb{R}^k$  because

$$\left\| \sum_{j=1}^k a_j \psi_h^j \right\|_{\mathbb{U}}^2 = \sum_{j=1}^k a_j^2 =: \|\mathbf{a}\|_2^2, \quad \mathbf{a} \in \mathbb{R}^k. \quad (3.31)$$

In other words, the estimator respects the intrinsic problem metrics which is a major difference from common approaches involving neural networks.

As argued earlier, we wish to construct a nonlinear map that recovers from data  $w \in \mathbb{W}_h$  a state  $w + B(w) \in w + \widetilde{\mathbb{W}}_h^\perp$  for an appropriate  $B : \mathbb{W}_h \rightarrow \widetilde{\mathbb{W}}_h^\perp$ . More specifically, for any  $w_h = \sum_{i=1}^m w_i \phi_h^i =: \mathbf{w}^\top \Phi \in \mathbb{W}_h$ , the envisaged mapping  $B$  has the form

$$B(w_h) = \mathbf{w}_\perp(\mathbf{w})^\top \Psi, \quad (3.32)$$

where

$$\mathbf{w}_\perp(\mathbf{w}) = (w_{\perp,h}^1(\mathbf{w}), \dots, w_{\perp,h}^k(\mathbf{w}))^\top \in \mathbb{R}^k, \quad (3.33)$$

and

$$\mathbf{w}_\perp(\mathbf{w}) = \mathcal{NN}(\mathbf{w}) \quad (3.34)$$

will be represented as a neural network with input data  $\mathbf{w} \in \mathbb{R}^m$  and output dimension  $k$ .

**(4) Loss Function and Training the Neural Network (NN):** We randomly select a subset  $\mathcal{U}_{train} = \{u_h^1, \dots, u_h^{N_{train}}\}$  from the “truth” FE data  $\mathcal{U}_{sample} = \{u_h^s : s = 1, \dots, \hat{N}\}$ , generated in step (1), for training purpose and leave the rest  $\mathcal{U}_{ghost} := \mathcal{U}_{sample} \setminus \mathcal{U}_{train}$  for testing. The associated coefficient vectors  $\{\mathbf{w}^1, \dots, \mathbf{w}^{N_{train}}\}$  and  $\{\mathbf{c}^1, \dots, \mathbf{c}^{N_{train}}\}$  are used as the training data for minimizing the natural empirical loss analogous to (2.19)

$$\text{Loss} = R(\Theta) := \frac{1}{N_{train}} \sum_{t=1}^{N_{train}} \|\mathbf{c}^t - \mathcal{NN}(\mathbf{w}^t; \Theta)\|_2^2, \quad (3.35)$$

where we assume in what follows that the  $\mathcal{NN}$  depends on a collection  $\Theta$  of *trainable* or *hyperparameters*, over which **Loss** is to be minimized.

Once the training of  $\mathcal{NN}$  is completed, for any new measurement  $\ell(u(\cdot, \mathbf{y}))$  with coefficient vector  $\mathbf{w} \in \mathbb{R}^m$ , defined by (3.23), (3.24), the observed state  $u(\cdot, \mathbf{y})$  is approximated by

$$u \approx \Phi_h^\top \mathbf{w} + \Psi_h^\top \mathcal{NN}(\mathbf{w}).$$

A natural question would be now to analyze the performance of the estimator obtained by minimizing the loss. This could be approached by employing standard machine learning concepts like Rademacher complexity in conjunction with more specific assumptions on the network structure and the solution manifold. We postpone this task to forthcoming work and address in the remainder of this paper instead a more elementary issue, namely “optimization success” which is most essential for a potential merit of the proposed schemes.

### 3.2 A Closer Look at Step (4)

It is a priori unclear which specific network architecture and which budget of trainable parameters is appropriate for the given recovery problem. Even if such structural knowledge were available, it is not clear whether the expressive potential of a given network class can be exhausted by the available standard optimization tools largely relying on stochastic gradient descent (SGD) concepts. Aside from formulating a model-compliant regression problem, our second primary goal is

to explore numerical strategies that, on the one hand, render optimization stable and less sensitive on algorithmic settings whose most favorable choice is usually not known in practice. On the other hand, we wish to incorporate and test some simple mechanisms to *adapt* the network architecture, inspired by classical “nested iteration” concepts in numerical analysis. Corresponding simple mechanisms can be summarized as follows: (a) A ResNet architecture (RNN) with its skip-connections is known to mitigate “gradient damping” which impedes the adjustment of trainable parameters in lower blocks when using deep networks. (b) Each block in an RNN can be viewed as a perturbation of the identity and may therefore be expected to support a stable incremental accuracy upgrade. (c) Instead of “plain training” of an RNN, where SGD is applied to all trainable parameters simultaneously, we study an iterative sweeping strategy that optimizes only single blocks at a time while freezing trainable parameters in all other blocks. Part of the underlying rationale is that training a shallow is more reliable and efficient than training a deep network. We discuss these issues next in more detail.

**Neural Network Setting:** Specifically, we consider the following *Residual Neural Network* (RNN) structure with  $i$  blocks:

$$\mathcal{NN}^{[i]}(\mathbf{x}; \theta^{[0]}, \theta^{[1]}, \dots, \theta^{[i]}) := \mathcal{N}^{[i]}(\mathcal{NN}^{[i-1]}(\mathbf{x}; \theta^{[0]}, \theta^{[1]}, \dots, \theta^{[i-1]}); \theta^{[i]}). \quad (3.36)$$

with each block defined by

$$\begin{aligned} \mathcal{N}^{[1]}(\mathbf{x}; \theta^{[0]}, \theta^{[1]}) &:= W_3^{[1]} \sigma(W_2^{[1]} \sigma(W_1^{[1]} \mathbf{x} + b_1^{[1]}) + b_2^{[1]}) + W^{[0]} \mathbf{x}, \\ \mathcal{N}^{[i]}(\mathbf{x}, \theta^{[i]}) &:= W_3^{[i]} \sigma(W_2^{[i]} \sigma(W_1^{[i]} \mathbf{x} + b_1^{[i]}) + b_2^{[i]}) + \mathbf{x}, \quad i = 2, 3, \dots \end{aligned}$$

where  $\theta^{[i]} = \{W_1^{[i]}, W_2^{[i]}, W_3^{[i]}, b_1^{[i]}, b_2^{[i]}\}$  for  $i = 1, 2, \dots$  and  $\theta^{[0]} = \{W^{[0]}\}$ ,  $\sigma(\cdot)$  is some pointwise nonlinear function (see Figure 3 for an descriptive diagram of the RNN structure).

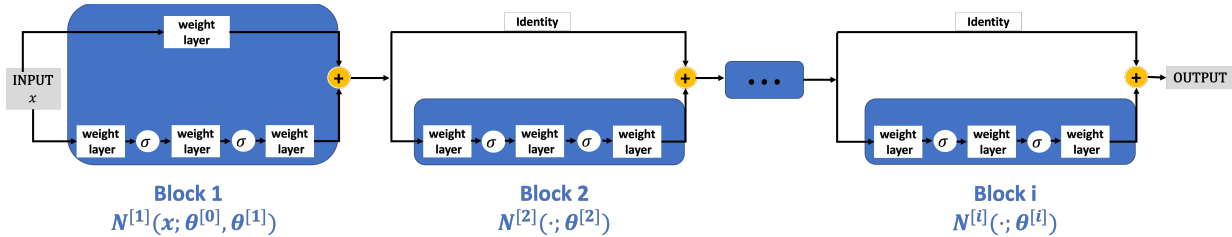


Figure 3: ResNet with  $i$  blocks

**An Expansion Strategy:** As indicated earlier, we will not approximate the recovery map using a fixed network architecture. We rather start with training a single hidden layer until saturation. We then proceed approximating residual data with another shallow network, and iterate this process which results in a ResNet structure. The basic rationale is similar to “full multigrid” or “nested iteration” in numerical analysis.

To describe the procedure in more detail, let

$$\mathcal{D} := \{\mathbf{w}^i : i = 1, \dots, N^{train}\} \times \{\mathbf{c}^i : i = 1, \dots, N^{train}\}$$

denote the set of training data, as described before. In view of (3.31), we employ simple mean-squared loss functions. In these terms we may rewrite (3.35) as

$$\mathcal{L}_{\mathcal{D}}[f] := \frac{1}{\#\mathcal{D}} \sum_{(\mathbf{w}, \mathbf{c}) \in \mathcal{D}} \|\mathbf{c} - f(\mathbf{w})\|_2^2. \quad (3.37)$$

In these terms, the procedure can be described as follows: At the initial step  $f$  is taken as a shallow network  $\mathcal{NN}^{[1]}(\cdot; \theta^{[0]}, \theta^{[1]})$  and solve first the optimization problem:

$$\mathbf{OP-1} : \min_{(\theta^{[0]}, \theta^{[1]}) \in \Theta^{[1]}} \mathcal{L}_{\mathcal{D}}[\mathcal{NN}^{[1]}(\cdot; \theta^{[0]}, \theta^{[1]})],$$

where  $\Theta^{[1]}$  denotes the budget of hyper-parameters used at this first stage, encoding in particular, the widths. **OP-1** is treated using standard stochastic gradient descent (SGD) until the loss stagnates or reaches a (local) minimum. The resulting hyper-parameters are denoted by  $(\theta_*^{[0]}, \theta_*^{[1]})$ .

In a next step, we expand the neural network by introducing a new block and solve

$$\mathbf{OP-2} : \min_{(\theta^{[0]}, \theta^{[1]}, \theta^{[2]}) \in \Theta^{[2]}} \mathcal{L}_{\mathcal{D}}[\mathcal{NN}^{[2]}(\cdot; \theta^{[0]}, \theta^{[1]}, \theta^{[2]})],$$

over an extended global budget of hyper-parameters  $\Theta^{[2]}$ . Moreover, **OP-2** itself is solved by sweeping over sub-problems as follows. Fixing the values of the trained parameters  $\theta^{[1]} = \theta_*^{[1]}$  and  $\theta^{[0]} = \theta_*^{[0]}$  we apply gradient descent first only over the newly added trainable parameters  $\theta^{[2]}$ . That is, we solve,

$$\mathbf{OP-2}^* : \min_{\theta^{[2]}} \mathcal{L}_{\mathcal{D}}[\mathcal{NN}^{[2]}(\cdot; \theta_*^{[0]}, \theta_*^{[1]}, \theta^{[2]})].$$

Due to the RNN structure, upon defining the data

$$\mathcal{D}_1 := \{(\mathcal{NN}^{[1]}(\mathbf{w}; \theta_*^{[0]}, \theta_*^{[1]}), \mathbf{c} - \mathcal{NN}^{[1]}(\mathbf{w}; \theta_*^{[0]}, \theta_*^{[1]})) \mid (\mathbf{w}, \mathbf{c}) \in \mathcal{D}\},$$

this is equivalent to optimizing

$$\min_{\theta^{[2]}} \mathcal{L}_{\mathcal{D}_1}[\mathcal{NN}^{[2]}(\cdot; \theta^{[2]})]$$

with a  $\mathcal{NN}^{[1]}$  – projected input and a residual from **OP-1** as output.

We can thus expect  $\mathcal{NN}^{[2]}$  to perform better than  $\mathcal{NN}^{[1]}$  in terms of learning the map between the observation  $\mathbf{w}$  and state-labels  $\mathbf{c}$  because adding an approximate residual presumably increases the overall accuracy of the estimator.

Once a new block has been added, the parameters in preceding blocks presumably could be further adjusted. This can be done by repeating a sweep over all blocks, i.e., successively optimizing each block while freezing the hyper-parameters in all remaining blocks.

The retained ghost-samples in  $\mathcal{U}_{ghost}$  can now be used to assess the generalization error. If this is found unsatisfactory, the current RNN can be expanded by a further block, leading to analogous optimization tasks **OP-k**. Moreover, for  $k > 2$ , the advantages of training shallow networks can be exploited by performing analogous block-optimization steps freezing the hyper-parameters in all but one block. In addition, we are free to design various more elaborate sweeping strategies.

For instance, one could include a simultaneous optimization over all trainable parameters at the end of the training process. We refer to §5.4 for related experiments.

Another way of viewing this process is to consider the infinite optimization problem

$$\mathbf{OP}: \quad \min_{\theta \in \mathbb{R}^\infty} \mathcal{L}_D[\mathcal{NN}(\cdot; \theta)].$$

where  $\mathcal{NN}(\cdot; \theta) := \lim_i \mathcal{NN}^{[i]}(\cdot; \theta^{[0]}, \theta^{[1]}, \dots, \theta^{[i]})$  is an idealized RNN with an infinite number of blocks. Then the above block expanding scheme can be interpreted as a greedy algorithm for approximately solving the infinite problem **OP**

$$\mathbf{OP-i} = \min_{\theta^{[0]}, \theta^{[1]}, \dots, \theta^{[i]}} \mathcal{L}_D[\mathcal{NN}(\cdot; \theta^{[0]}, \theta^{[1]}, \dots, \theta^{[i]}, \mathbf{0})].$$

successively increasing  $i$  until the test on ghost-samples falls below a set tolerance.

In Section 6, we will first present the accuracy of the recovered solutions with the **nonlinear** map learned with a RNN compared to solutions obtained with the Reduced Basis Method (RBM). We showed that in piece-wise constant case, RNN can reach similar accuracy as RBM. In log-normal case, while the RBM can not be applied to obtain reasonable solutions, we showed that RNN can still be used to obtain a nonlinear solution with  $L_2$  lifting (see Section 4.2).

## 4 Numerical Results

The above description of a state estimation algorithm is so far merely a skeleton. Concrete realizations require fixing concrete algorithmic ingredients such as batch sizes, and learning rates in SGD sweeps or the number of block-sweeps at the various expansion stages. The numerical experiments reported in this section have two major purposes: (I) shed some light on the following issues: dependence of optimization success on these ingredients, especially in comparison with a “one-shot” global optimization, the ability to reach near-minima, and the stability of the scheme; a central issue concerns comparisons between blockwise sweeping (eRNN) and plain global training (RNN); (II) compare the performance of neural networks with estimators that are based on Reduced Basis concepts for Scenario (S1) of piecewise constant affine parameter representations of the diffusion coefficients, introduced in §2.1. (S1) is known to be a very favorable scenario for Reduced Basis methods that have been well studied for this kind of problems exhibiting excellent performance, [4, 6].

We wish to estimate the relative analogue to the ideal regression risk (2.19):

$$\mathcal{E} := \left( \frac{\mathbb{E}_{\mathbf{y} \in \mathcal{Y}_{test}} \|u(\mathbf{y}) - u_{pred}(\mathbf{y})\|_{\mathbb{U}}^2}{\mathbb{E}_{\mathbf{y} \in \mathcal{Y}_{test}} \|u(\mathbf{y})\|_{\mathbb{U}}^2} \right)^{\frac{1}{2}},$$

where  $u_{pred} := \Phi_h \mathbf{w} + \Psi_h \mathbf{c}_{pred}$ . In particular, if the norm is taken to be the problem compliant norm  $\|\cdot\|_{\mathbb{U}}$ , due to Remark 1, evaluating its empirical counter part:

$$\hat{\mathcal{E}} = \left( \frac{\sum_s \|\mathbf{c}^s - \mathbf{c}_{pred}^s\|_2^2}{\sum_s \|\mathbf{w}\|_2^2 + \|\mathbf{c}^s\|_2^2} \right)^{\frac{1}{2}}.$$

just requires computing Euclidean norms for the predicted coefficients  $\{\mathbf{c}_{pred}^s\}$ . Of course, we expect sufficient large sample sizes provide accurate estimates

$$\hat{\mathcal{E}} \approx \mathcal{E}.$$

If one would like to evaluate the accuracy of the recovered solution  $u_{pred}(\mathbf{y})$  in a norm that is different form the natural norm ( $\|\cdot\|_{\mathbb{U}}$ ), quadrature in the truth space  $\mathbb{U}_h$  is required to approximately evaluate the respective norm of the functions.

Furthermore, we explore the performance of the RNN-based estimator for scenario (S2), involving log-normal random diffusion parameters. In this case the performance of Reduced Basis is much less understood and hard to certify. Corresponding experiments are discussed in Section 4.2. To ease the description of the experiment configurations, we list the notations in Table 1.

Abbreviation	Explanation	Comments
RNN	Residual neural network	
eRNN	Expanded RNN	Residual blocks added and trained sequentially
B	Number of blocks	
W	Width of hidden layers	Random parameter initialization drawn from a Gaussian distribution
O	Output dimension of $\mathbf{c}$	Number of orthogonal basis taken in $\tilde{\mathbb{W}}_h^\perp$
l	$l^1$ regularization weight of trainable learning parameters	0.00001 if not specified
b	Batch size	100 if not specified
lr	Learning rate	
Train	Training data type	
pwc	Piecewise constant case training set (S1)	10,000 samples subject to 16 uniformly distributed sensors
log-normal	Log-normal case training data (S2)	1,000 samples when 16 sensors; 5,000 samples when 49 sensors
sen	Number of uniformly distributed sensors	
POD- $H^1$	Dimension reduction of $\tilde{\mathbb{W}}_h^\perp$ with POD in $H^1$ sense	
POD- $L_2$	Dimension reduction of $\tilde{\mathbb{W}}_h^\perp$ with POD in $L_2$ sense	

Table 1: Abbreviations

## 4.1 The Piecewise Constant Case (S1)

We first consider the aforementioned diffusion problem (2.5) with  $f = 1$  and a piecewise constant diffusive parameter within  $\Omega = [0, 1]^2$ . More specifically, we consider a non-overlapping,  $4 \times 4$  uniform decomposition  $\{\Omega_j\}_{j=1}^{16}$  of  $\Omega$ . The diffusion coefficient is a constant on each  $\Omega_j$  as defined in (2.7) .

#### 4.1.1 RNN vs. eRNN

The first group of experiments concerns a general performance comparison between the ResNet expansion strategy - in short eRNN, outlined above and standard SGD techniques applied to the whole network with the same architecture, termed RNN in what follows. By “performance” we mean training efficiency as well as corresponding achieved training and generalization losses. Specifically, we consider first the case where  $m = 16$  sensors are placed uniformly in  $\Omega$  (see Figure 4) and the corresponding measurements are evaluated by averaging the solution at the four vertices of a square of side 0.001 centered at the sensor location, see (3.26). Thus, the number of sensors equals in this case the parametric dimension so that there is a chance that the measurements determine the state uniquely.

We use in total 10,000 snapshots represented in the truth-space that serve as synthetic data, 500 of which are used for testing purposes. To draw theoretical conclusions a larger amount of test data would be necessary. However, intense testing has revealed that larger test sizes have no significant effect on the results in the scenarios under consideration. Based on computations, using these data we find that  $k = 28$  basis functions suffice to reserve 99.5% of the  $H^1$ -energy in  $\widetilde{\mathbb{W}}_h^\perp$ , represented by the Hilbert-Schmidt norm of a full orthonormal basis in  $\widetilde{\mathbb{W}}_h^\perp$ . The case studies documented by subsequent figures are referenced as follows: “pwc” refers to “piecewise constant diffusion coefficients” in scenario (S1); “POD- $H^1$ ” indicates that the sensors have been Riesz-lifted to  $H^1(\Omega)$  which accommodates the measurement space  $\mathbb{W}$ . The SVD truncation threshold is chosen to ensure accuracy in  $H^1(\Omega)$ ; recall also that “sen16” means that the recovery is based on data from 16 sensors.

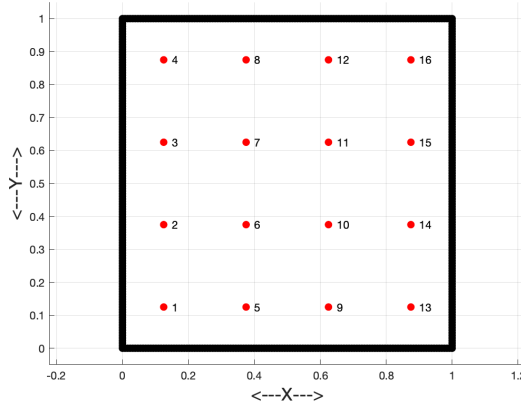


Figure 4: 16 uniformly distributed sensors.

The numerical results, shown in Figure 5, indicate that the training loss resulting from eRNN decays faster than the standard RNN training in this case. The relative generalization errors for both approaches after  $12 \times 10^5$  steps of training are displayed in Table 2, where the generalization errors are evaluated on the test set of 500 samples. The result shows that eRNN outperforms RNN in a sense detailed later below. In particular, the training loss for eRNN drops faster to a saturation level which can be achieved by RNN only at the expense of a significantly larger

training effort. We also compare the estimated generalization error in  $H^1$  with the achieved (expectedly smaller) error in the weaker  $L_2$ -norm.

One observes though that increasing network depth, i.e., employing a higher number of ResNet blocks does not increase accuracy significantly in either model. This indicates that a moderate level of nonlinearity suffices in this scenario. This is not surprising considering the moderate number of POD basis functions needed to accurately capture complement information.

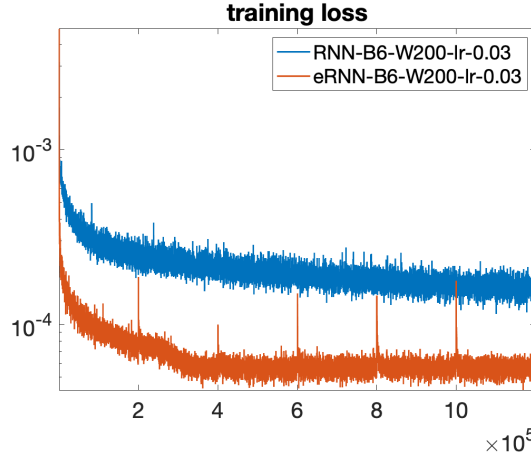


Figure 5: **eRNN/RNN training loss comparison.** Train-*pwc-sen16-POD- $H^1$* , B6-W200-O28-lr0.03.

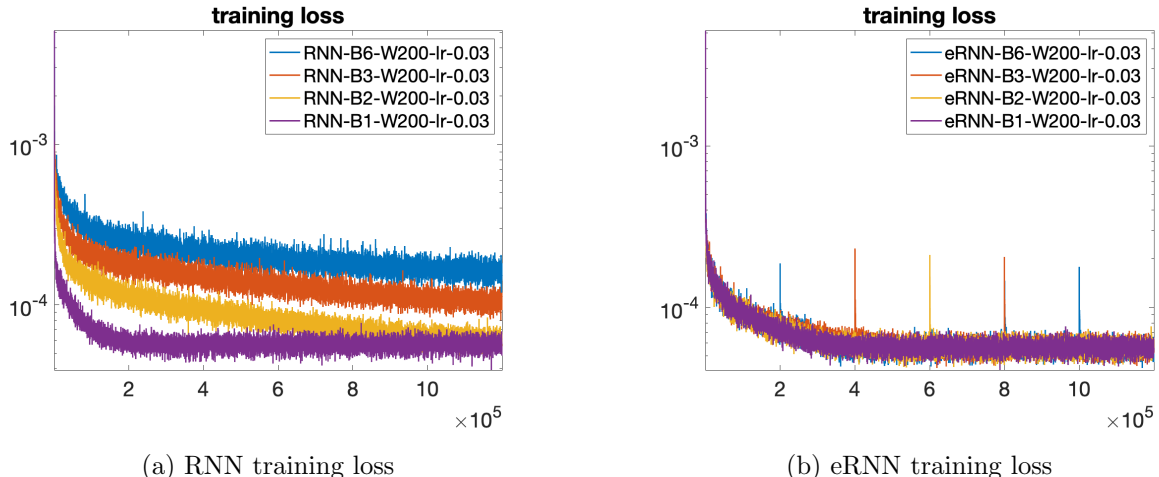


Figure 6: **Training loss of RNN/eRNN v.s. different number of Blocks.** Train-*pwc-sen16-POD- $H^1$* , W200-O28-lr0.03.

# of blocks	#of trainable	$\hat{\mathcal{E}}$		Relative $L_2$ Error of $u_{pred}$	
		eRNN	RNN	eRNN	RNN
1	49,648	9.76%	9.76%	3.01%	3.01%
2	101,248	9.77%	10.13%	3.01%	3.13%
3	152,848	9.76%	13.53%	3.01%	4.09%
6	307,648	9.78%	16.85%	3.01%	5.27%

Table 2: **Generalization error v.s. different number of ResNet blocks (fixed total training steps  $12 \times 10^5$ ).** Train-*pwc-sen16-POD- $H^1$* , eRNN/RNN-W200-O28-Ir0.03.

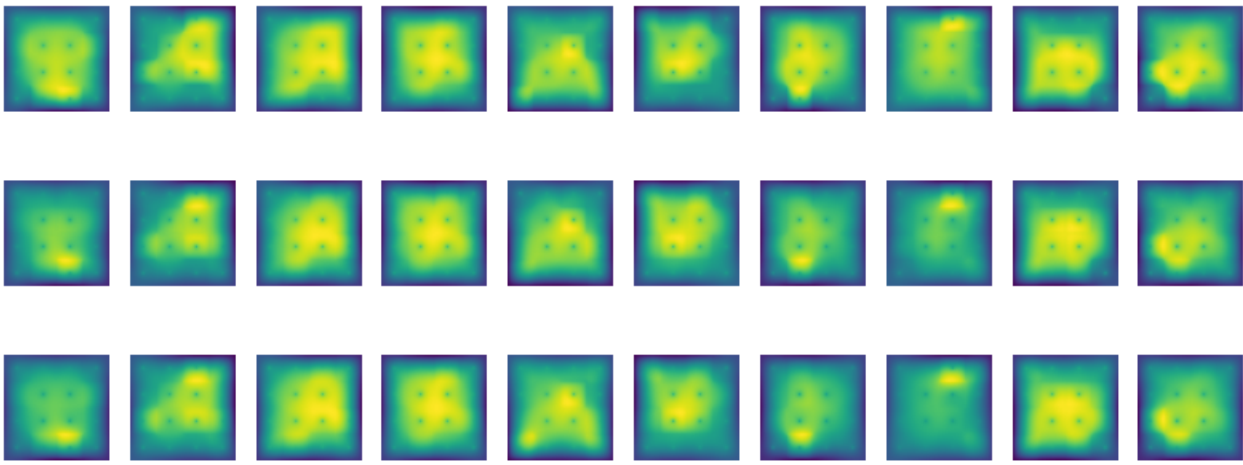


Figure 7: Train-*pwc-sen16-POD- $H^1$* , B6-W200-O28-Ir0.03. **Upper row:** reference projected solution  $z_h^s = P_{\tilde{\mathbb{W}}_h^\perp} u_h^s$ ; **Middle row:** Prediction of  $z_h^s$  with **RNN**; **Lower row:** Prediction of  $z_h^s$  with **eRNN**.

To conclude, our findings can be summarized as follows: When using larger widths, e.g. 200, eRNN leads to a faster convergence and a somewhat smaller generalization error in comparison with plain RNN training. In fact, while in eRNN the generalization error at least does not increase when increasing network complexity, plain RNN shows a degrading performance reflecting increasing difficulties in realizing expressive potential. On the other hand, for smaller widths, such as 20, the performance of both variants is comparable. It should be noted that already a single block and width = 20 achieves an ‘‘empirical accuracy level’’ that is improved only slightly by more complex networks (compare Table 2 with Table 3). A significant increase in the number of trainable parameters has not resulted in a significant decrease of training and generalization losses, indicating that standard SGD does not exhaust the expressive power of the underlying networks. This may rather indicate that larger neural network complexity widens a plateau of local minima of about the same magnitude in the loss landscape while parameter choices

realizing higher accuracy remain isolated and very hard to find. Of course, this could be affected by different (more expensive) modelities in running SGD which incidentally would change the implicit regularization mechanism.

# of blocks	#of trainable	$\hat{\mathcal{E}}$		Relative $L_2$ Error of $u_{pred}$	
		eRNN	RNN	eRNN	RNN
1	1,768	9.76%	9.76%	3.01%	3.01%
2	3,328	9.76%	9.76%	3.01%	3.01%
3	4,888	9.76%	9.77%	3.01%	3.01%
6	9,568	9.76%	9.76%	3.01%	3.01%

Table 3: **Generalization error v.s. different number of ResNet blocks (fixed total training steps  $12 \times 10^5$ ).** Train-*pwc-sen16-POD- $H^1$* , eRNN/RNN-W20-O28-*lr*0.03.

## 4.2 Log-normal case

As indicated earlier, uniform ellipticity in conjunction with affine parameter dependence of the diffusion coefficients offers very favorable conditions for the type of affine space recovery schemes described in Section 2.4. In particular, affine parameter dependence as well as rapidly decaying Kolmogorov  $n$ -widths (2.17) are quite important for methods, resorting to Reduced Bases, to work well, while neural networks are far less dependent on these preconditions. Therefore, we turn to scenario (S2) which is more challenging in both regards.

Specifically, we consider the case with  $a_0 = 0$  and  $a_1 = 1$  in (2.8). Recall that we aim to learn the map form  $\mathbf{w} \rightarrow \mathbf{c}$  where  $\mathbf{c}$  is the POD coefficient vector of the solution in  $\mathbb{W}_h^\perp$ .

First, since the diffusion coefficients no longer depend affinely on the parameters  $\mathbf{y}$ , rigorously founded error surrogates are no longer computable in an efficient way. This impedes the theoretical foundation as well as the efficiency of methods using Reduced Bases and therefore provides a strong motivation exploring alternate methods. Second, it is not clear whether the solution manifold  $\mathcal{M}$  still have rapidly decaying  $n$ -widths, so that affine spaces of moderate dimension will not give rise to accurate estimators. In fact, computing the SVD of the snapshot projections  $\{z_h^1, \dots, z_h^{\hat{N}}\}$ , based on the Riesz representations of the measurement functionals in  $\mathbb{U} = H^1$ , shows only very slowly decaying singular values. This indicates that  $P_{\mathbb{W}_h^\perp}(\mathcal{M})$  cannot be well approximated by a linear space of moderate dimension. Thus, when following the above lines, we would have to seek coefficient vectors  $\mathbf{c}$  in a space of dimension comparable to  $\hat{N}$ , which renders training RNN prohibitive. Finally, the diffusion coefficients may near-degenerate degrading uniform ellipticity. This raises the question whether  $H^1$  is still an appropriate space to accommodate a reasonable measurement space  $\mathbb{W}$  which is at the heart of the choice of sensor coordinates (2.12). These adverse effects are reflected by the numerical experiments discussed below.

Therefore, we choose in scenario (S2)  $\mathbb{U} = L_2(\Omega)$  which means we are content with a weaker metric for measuring accuracy. As a consequence, the representation of the functionals  $\ell(u)$  in

$L_2(\Omega)$  is the  $L_2$ -orthogonal projection of these functionals to the truth-space  $\mathbb{U}_h$  which then, as before, span the measurement space  $\mathbb{W}_h \subset \mathbb{U}_h$ . As indicated earlier, we give up on quantifiable gradient information but facilitate a more effective approximation of  $P_{\mathbb{W}_h^\perp}(\mathcal{M})$  where the projection is now understood in the  $L_2$ -sense. In fact, for  $\hat{N} = 1000$  snapshot samples, with the original  $H^1$ -Riesz-lifting, one needs the 1000 dominant POD modes to sustain 99.5% of the  $H^1$  energy. Instead, only 21 dominating modes are required to realize the same accuracy in  $L_2(\Omega)$ . All results presented in this section will be subject to this change. Nevertheless, for comparison we record below in each experiment also the relative  $H^1$ -error which, as expected, is larger by an order of magnitude.

#### 4.2.1 eRNN vs. RNN (16 sensors)

We are interested to see whether, or under which circumstances, the advantages of eRNN over plain RNN training persists also in scenario (S2) where several problem characteristics are quite different. We consider similar test conditions as before, namely 16 uniformly distributed sensors. In total, 1000 snapshots are collected providing 1000 synthetic data points, of which 950 are used for training while 50 are reserved for evaluation in this case. The dimension of observational data  $\mathbf{w}$  is then  $m = 16$ , while according to the preceding remarks, the effective complement space dimension, accommodating the coefficients  $\mathbf{c}$ , is  $k = 21$ .

The history of training losses is shown in Figure 8, where we observe again that the training of eRNN is more efficient than that of RNN. Specifically, when a new block is introduced in eRNN, the training loss decays more rapidly (see the corner of the loss curve in Figure 8 at step  $1 \times 10^5$ ). Thus, the expansion strategy is clearly beneficial in this case. Moreover, perhaps not surprisingly, we observe that RNN suffers from a slow down in loss decay when training a larger number of parameters simultaneously (Figure 9a). By contrast, for the block by block optimization in eRNN and fixed width, the number of simultaneously updated parameters stays constant so that even for larger (deeper) networks, one reaches a similar level of training loss at a smaller number of updates (see Figure 9b). Correspondingly, a slightly better overall accuracy of eRNN can be observed in terms of the generalization error (Table 4). One should keep in mind though that we have allotted a fixed budget of training steps to all variants in this experiment. Thus, increasing depth, reduces the training effort spent on each block which may explain the relatively large generalization error obtained for B12. Hence, when favoring accuracy improvements at the expense of more training steps, eRNN offers a clearly better potential while a global training seems to be rather limited. On the other hand, the results in Table 4 also indicate that not much gain in accuracy should be expected in this test case by using more than one or two blocks.

In summary, eRNN appears to offer advantages in training neural networks with larger depth compared with plain RNN. The relatively coarse information provided by the 16 measurement data seems to leave more room for an enhanced nonlinearity of deeper networks to capture the manifold component in  $\mathbb{W}^\perp$ . This will be seen in Section 4.2.2 to change somewhat when a larger number of sensors increases the accuracy of the “zero-order approximation” provided by

the projection  $P_{\mathbb{W}_h^\perp}$ .

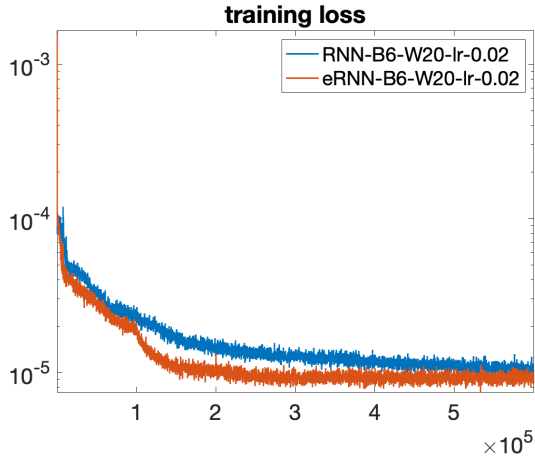


Figure 8: **eRNN/RNN training loss comparison.** Train-*log-normal-sen16-POD- $L_2$* , B6-W20-O21-lr0.02.

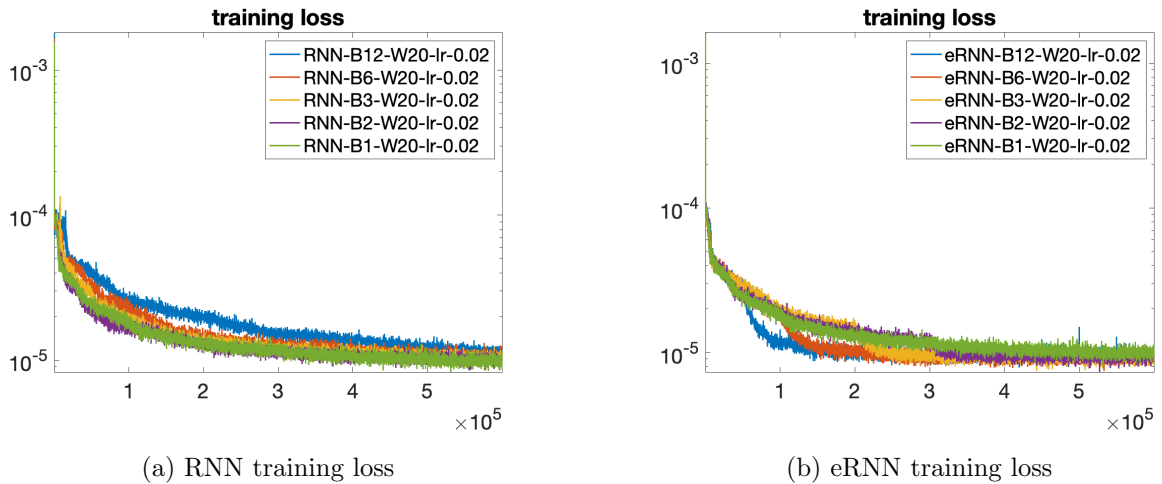


Figure 9: **Training loss of RNN/eRNN v.s. different number of Blocks.** Train-*log-normal-sen16-POD- $L_2$* , W20-O21-lr0.02.

#### 4.2.2 eRNN vs. RNN (49 sensors)

In this subsection, we consider 49 uniformly distributed sensors for measurements. In total, 6000 snapshots are collected. Among them, 5950 samples are used for training while 50 are reserved for evaluation. The dimension of the latent space accommodating  $\mathbf{c}^s$  is now  $k = 22$  after applying SVD and keeping 99.5% energy in the  $L_2$  sense.

However, in this case, from Figure 11, we can see that although the training loss of eRNN decays faster compared to RNN at the beginning, both ended up at a similar level. We also do not observe significant changes in decay rates of the loss when employing the expansion strategy

# of blocks	#of trainable	$\hat{\mathcal{E}}$		relative $H^1$ Error of $u_{pred}$	
		eRNN	RNN	eRNN	RNN
1	1,516	7.89%	7.89%	47.61%	47.61%
2	2,796	7.65%	7.94%	47.33%	48.26%
3	4,076	7.60%	8.00%	47.08%	48.31%
6	7,916	7.60%	8.12%	47.08%	48.65%
12	15,596	7.76%	8.42%	47.42%	49.28%

Table 4: **Generalization error v.s. different number of ResNet blocks (fixed total training steps  $6 \times 10^5$ ).** Train-*log-normal-sen16-POD- $L_2$* , eRNN/RNN-W20-O21-*lr*0.02.

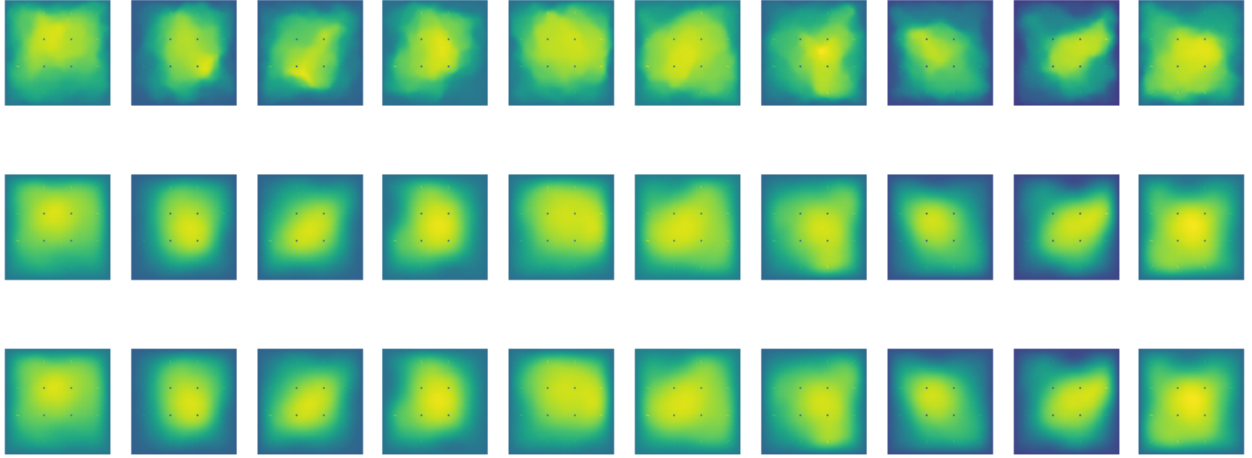


Figure 10: Train-*log-normal-sen16-POD- $L_2$* , B6-W20-O21-*lr*0.02. **Upper row:** reference projected solution  $z_h^s = P_{W_h^\perp} u_h^s$ ; **Middle row:** Prediction of  $z_h^s$  with **RNN**; **Lower row:** Prediction of  $z_h^s$  with **eRNN**.

eRNN (see Figure 11 at step  $6 \times 10^5$ ). In fact, the generalization error of eRNN is only slightly smaller than that of RNN (Table 5). In addition, it is seen that, within the given training budget, the best performance is already achieved using a shallow RNN. This indicates that, within the achievable accuracy range, the map of interest is close to a linear one, given that the “zero-order” approximation  $P_{W_h} u$  is now already rather accurate. However, we do notice that when applying a block by block training strategy in eRNN, while the difference in generalization error is small, the savings in training are huge because only one block is trained at a time, and thus the number of parameters under training is fixed. Thus, for deep neural networks, such a sequential training scheme is expected to be beneficial compared to updating all parameters simultaneously.

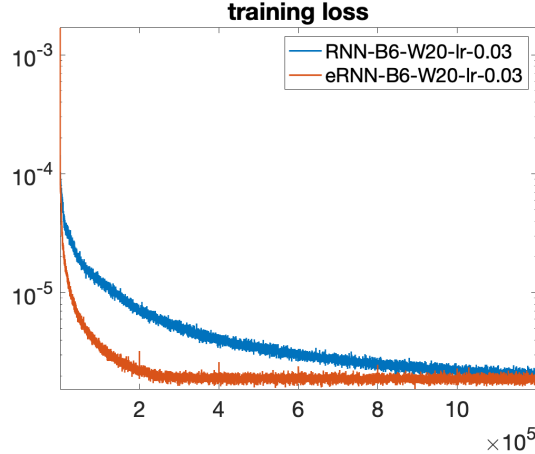


Figure 11: **eRNN/RNN training loss comparison.** Train-*log-normal-sen49-POD-L*<sub>2</sub>, B6-W20-O22-lr0.03.

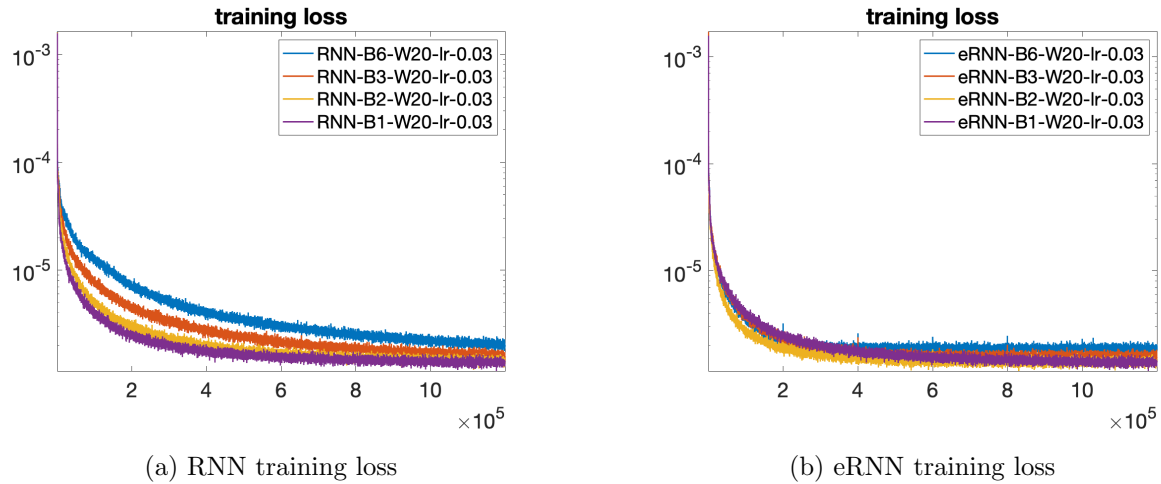


Figure 12: **Training loss of RNN/eRNN v.s. different number of Blocks.** Train-*log-normal-sen49-POD-L*<sub>2</sub>, W20-O22-lr0.03.

# of blocks	#of trainable	$\hat{\mathcal{E}}$		$H^1$ Error of $u_{pred}$	
		eRNN	RNN	eRNN	RNN
1	2,983	3.08%	3.08%	52.66%	52.66%
2	4,258	3.10%	3.13%	52.64%	52.71%
3	5,578	3.31%	3.34%	52.82%	53.06%
6	9,538	3.60%	3.69%	53.27%	53.90%

Table 5: **Generalization error v.s. different number of ResNet blocks (fixed total training steps  $12 \times 10^5$ ).** Train-*log-normal-sen49-POD-L*<sub>2</sub>, eRNN/RNN-W20-O22-lr0.03.

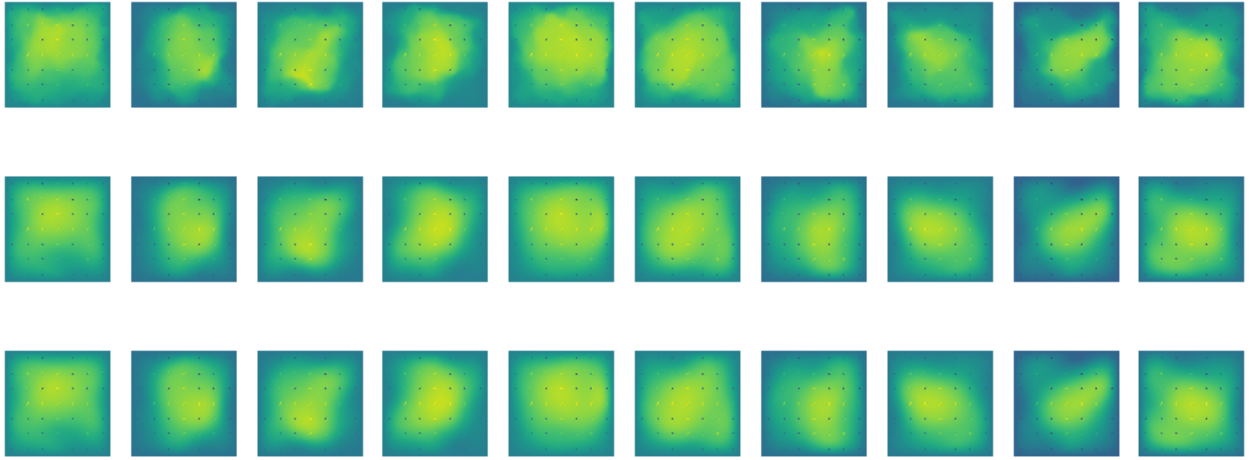


Figure 13: **Upper row:** reference projected solution  $z_h^s = P_{\mathbb{W}_h^\perp} u_h^s$ ; **Middle row:** Prediction of the  $z_h^s$  with **RNN**; **Lower row:** Prediction of  $z_h^s$  with **eRNN**.

## 5 Robustness of eRNN With Regard to Algorithmic Settings

In this section we further examine how sensitively eRNN depends on various algorithmic settings such as different learning rates or neural network architecture. We also wish to see whether extra steps of optimization over all trainable parameters can improve the overall performance, especially the generalization accuracy of eRNN. To be consistent, we stick to the example in Section 4.2.1, where a log-normal case is considered and 16 uniformly placed sensors give rise to the space  $\mathbb{W}_h$  and the corresponding complement  $\mathbb{W}_h^T$  in the truth space  $\mathbb{U}_h$ .

### 5.1 Sensitivity to Learning Rate

We first check how keeping learning rates constant, affects the performance of eRNN in comparison with RNN. Corresponding findings can be summarized as follows (see Figure 14 and Table 6):

- The training loss of eRNN converges faster for a wide range of *constant* learning rates.
- The generalization errors for eRNN are smaller.
- RNN could benefit from a decaying learning rate, while eRNN can perform better with constant learning rate which renders the scheme less dependent on the suitability of such hyper-parameter choices.

lr	$\hat{\mathcal{E}}$		Relative $H^1$ Error of $u_{pred}$	
	eRNN	RNN	eRNN	RNN
0.002	10.75%	14.50%	54.25%	61.29%
0.02	7.60%	8.00%	47.08%	48.31%
0.2	14.78%	16.66%	60.62%	62.96%

lr	$\hat{\mathcal{E}}$		Relative $H^1$ Error of $u_{pred}$	
	eRNN	RNN	eRNN	RNN
0.002	11.76%	13.38%	55.66%	60.13%
0.02	7.60%	8.12%	47.08%	48.65%
0.2	14.53%	23.44%	60.80%	76.68%

(b) B6

Table 6: **Generalization error v.s. different learning rates (fixed total training steps  $6 \times 10^5$ ).** Train-*log-normal*-sen16-POD- $L_2$ , W20-O21.

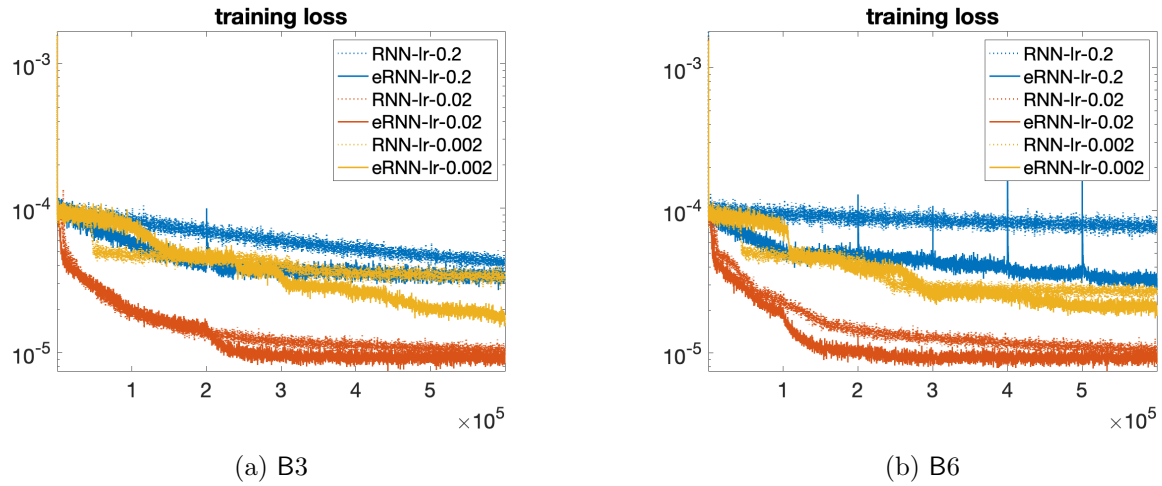


Figure 14: **Training loss of RNN/eRNN v.s. different learning rate.** Train-*log-normal*-sen16-POD- $L_2$ , W20-O21

## 5.2 Dependence on Neural Network Architecture

In this Subsection we explore the effect of varying the architecture again for the application in scenario (S2).

### 5.2.1 Width

As indicated by Figure 15 and as expected, neural networks of equal depth but larger widths require more training iterations to converge and each update is computationally more intense than for narrow ones. For both narrow and wide neural networks, eRNN appears to entail a

faster decay of the loss during the training process as well as a more accurate prediction.

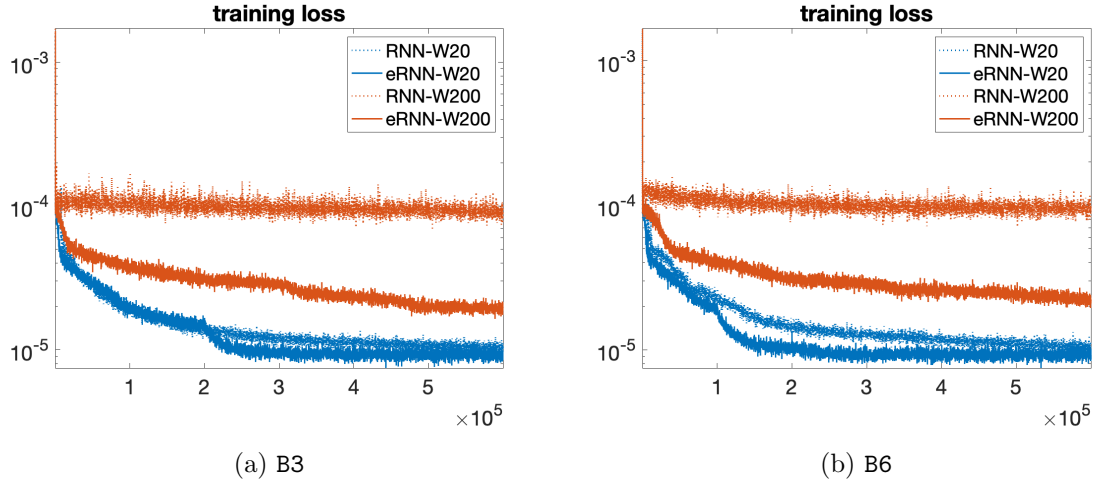


Figure 15: **Training loss of RNN/eRNN v.s. different width.** Train-*log-normal-sen16-POD- $L_2$* , O21-lr0.02

Width	$\hat{\mathcal{E}}$		Relative $H^1$ Error of $u_{pred}$	
	eRNN	RNN	eRNN	RNN
W20	7.60%	8.00%	47.08%	48.31%
W200	11.41%	25.10%	55.17%	77.85%

Width	$\hat{\mathcal{E}}$		Relative $H^1$ Error of $u_{pred}$	
	eRNN	RNN	eRNN	RNN
W20	7.60%	8.12%	47.08%	48.65%
W200	12.06%	24.94%	56.24%	75.99%

(b) B6

Table 7: **Generalization error v.s. different neural network width (fixed total training steps  $6 \times 10^5$ ).** Train-*log-normal-sen16-POD- $L_2$* , O21-lr0.02.

### 5.2.2 Dependence on Depth

Similar to what can be observed from Figure 9, we observe that, for the given test problems, deeper eRNNs can converge at a similar rate as shallower ones. By contrast, perhaps not surprisingly, the convergence of plain RNNs will generally slow down as depth increases. In other words, the deeper, the slower is the convergence of RNN. see Figure 16.

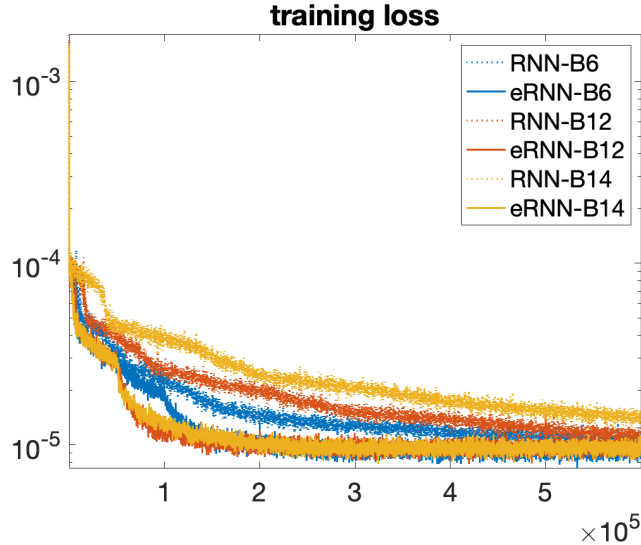


Figure 16: **Training loss of RNN/eRNN v.s. different depth (# of blocks).** Train-*log-normal-sen16-POD- $L_2$* , W20-O21-lr0.02

# of Blocks	$\hat{\mathcal{E}}$		Relative $H^1$ Error of $u_{pred}$	
	eRNN	RNN	eRNN	RNN
B6	7.60%	8.12%	47.08%	48.65%
B12	7.76%	8.42%	47.42%	49.28%
B14	8.17%	9.40%	47.78%	51.00%

Table 8: **Generalization error v.s. different number of ResNet blocks (fixed total training steps  $6 \times 10^5$ ).** Train-*log-normal-sen16-POD- $L_2$* , W20-O21-lr0.02.

### 5.3 Duration of Training

The above discussion of the influence of width and depth on the learning outcome is based on an assumption that a fixed training budget (# of SDG updates) is allowed. It is, in general, completely unclear whether such a budget suffices to exploit the expressive power of the network. We are therefore interested to see how eRNN and RNN compare when lifting the complexity constraints. This is the more interesting as an optimization step on a single block is not quite comparable with a descent step over the whole network. This discrepancy increases of course with increasing depth. As a first step in this direction, we inspect the effect of quadrupling the training budget using  $2.4 \times 10^6$ .

It turns out that earlier findings are confirmed. Eventually, given enough training time and effort, RNN can achieve about the same accuracy as eRNN which indicates that the “achievable” expressivity offered by the RNN architecture has been exploited by both optimization strategies. There is a slight gain of accuracy in comparison with the previous cap of  $6 \times 10^5$ , namely  $0.02\% \sim 0.03\%$ .

	$\hat{\mathcal{E}}$		Relative $H^1$ Error of $u_{pred}$	
	eRNN	RNN	eRNN	RNN
Total training steps				
$6 \times 10^5$	7.60%	8.12%	47.08%	48.65%
$24 \times 10^5$	7.75%	7.74%	47.10%	47.09%

Table 9: **Generalization error v.s. different number of training steps.** Train-*log-normal*-sen16-POD- $L_2$ , B6-W20-O21- $\text{lr}0.02$ .

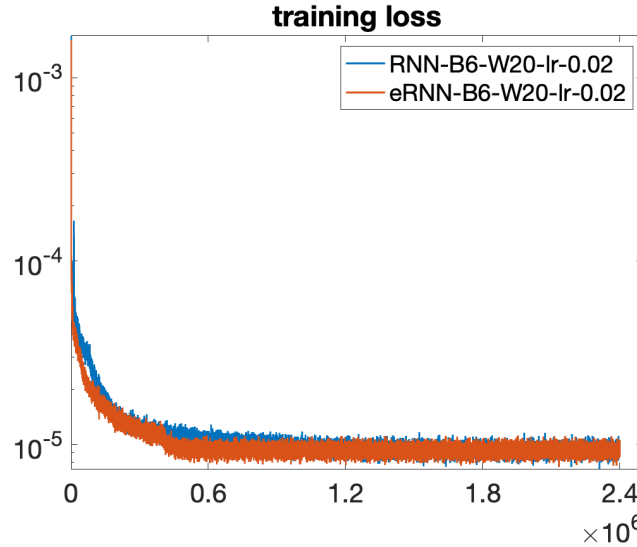


Figure 17: **Training loss of RNN/eRNN for large number of training steps ( $2.4 \times 10^6$ ).** Train-*log-normal*-sen16-POD- $L_2$ , B6-W20-O21- $\text{lr}0.02$

#### 5.4 Training Schedules

In this example, we add an additional  $2 \times 10^5$  training steps to update all trainable parameter simultaneously. Compared with a pure block by block training schedule (see Figure 8), the additional global optimization effort does not seem to improve on the training success but rather worsens it (see Figure 18).

	$\hat{\mathcal{E}}$		Relative $H^1$ Error of $u_{pred}$	
	eRNN	RNN	eRNN	RNN
Total training steps				
$6 \times 10^5$ block-wise updates	7.60%	8.12%	47.08%	48.65%
$6 \times 10^5$ block-wise updates + $2 \times 10^5$ global updates	7.75%	7.99%	47.10%	47.91%

Table 10: **Generalization error with/without  $2 \times 10^5$  global updates.** Train-*log-normal*-sen16-POD- $L_2$ , B6-W20-O21- $\text{lr}0.02$ .

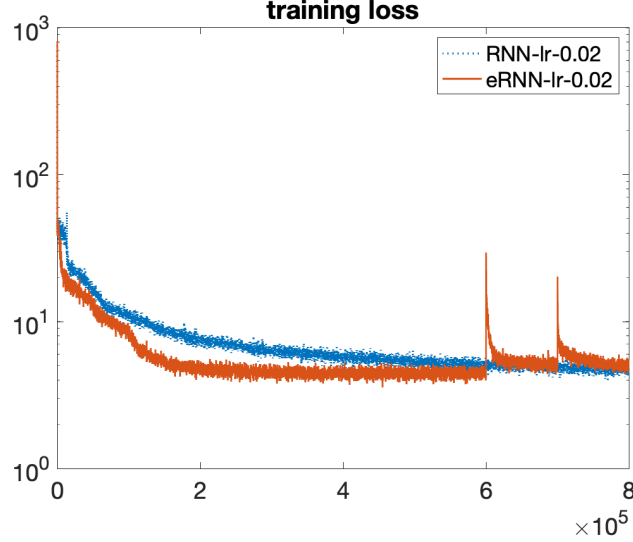


Figure 18: **Training loss of RNN/eRNN with  $2 \times 10^5$  steps of global updates.** Train-*log-normal-sen16-POD- $L_2$* , B6-W20-O21-Ir0.02

## 5.5 Wide Neural Network Subject to Long-term Training

We check at last whether the neural networks can do better than in previous experiments in terms of approximating the map between  $\mathbb{W}_h$  and  $\mathbb{W}_h^\perp$  when significantly increasing training time. The

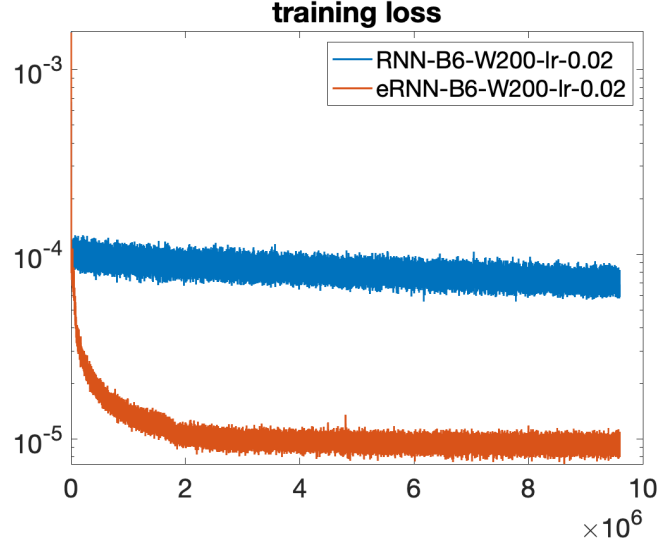


Figure 19: **Training loss of RNN/eRNN for large number of training steps ( $9.6 \times 10^6$ ) of wide neural network (W200).** Train-*log-normal-sen16-POD- $L_2$* , B6-W200-O21-Ir0.02

results show that earlier findings persist. Table 11 shows that, while with eRNN there is no real benefit of larger width, at least estimation quality does not appear to degrade over long training periods. Instead, RNN seems to be adversely affected by larger network complexity.

Total training steps	$\hat{\mathcal{E}}$		Relative $H^1$ Error of $u_{pred}$	
	eRNN	RNN	eRNN	RNN
short ( $6 \times 10^5$ ) & narrow (W20)	7.60%	8.12%	47.08%	48.65%
long ( $24 \times 10^5$ ) & narrow (W20)	7.75%	7.74%	47.10%	47.09%
short ( $6 \times 10^5$ ) & wide (W200)	12.06%	24.94%	56.24%	75.99%
long ( $24 \times 10^5$ ) & wide (W200)	8.82%	23.09%	49.66%	78.19%
super long ( $96 \times 10^5$ ) & wide (W200)	7.77%	21.83%	47.17%	71.95%

Table 11: **Generalization error v.s. different number of training steps.** Train-*log-normal-sen16-POD- $L_2$* , B6-O21-*lr*0.02.

More specifically, Table 11 shows that the smallest generalization error is achieved by the relatively low training effort for narrow networks. Much larger networks, instead, seem to achieve about that same accuracy level only at the expense of a significantly larger training effort, leaving little hope for substantial further accuracy improvements by continued training. In contrast, globally updating corresponding networks achieves the best result again for narrow networks but, in agreement with earlier tests, at the expense of four times as many training steps than for block-wise training schedules. For wide networks even extensive training effort does not seem to reproduce accuracy levels, achieved earlier for smaller networks.

## 6 Comparison with Affine Reduced Basis Estimators

As discussed earlier in more detail, we have run these experiments with varying choices of learning rates and architecture modifications consistently obtaining essentially the same magnitude of training loss and generalization error. This indicates a certain saturation effect as well as reliability in generating consistent results. Nevertheless, one wonders to what extent the actual expressive power of the networks is at least nearly exhausted and how to gauge the results in comparison with alternate approaches. We have therefore compared the accuracy achieved by eRNN with results for Affine Space estimators from [5], mentioned earlier in Section 2.4. For the sake of such a comparison we consider the same type of up to 50 randomly distributed sensors depicted in Figure 20). We generate again 10,000 data points 9000 of which are used for training while the rest is used for evaluation. Based on the experiences gained in previous experiments we have used a B2-W100 eRNN as a model for learning the observation-to-state mapping. That is, the RNN of 2 blocks is trained in the expansion manner. We confine the training of the eRNN to a fixed number of 100,000 steps. The dependence of the tested generalization error on the number of sensors is shown in Figure 22. As expected, an increasing number of sensors provides more detailed information on  $P_{\tilde{W}_h^\perp}(\mathcal{M})$ . The green and blue curve show that further increasing the number of training data has little effect on the achieved accuracy. For the given fixed budget of 10,000 steps the evaluation shows an  $H^1$ -error of about  $10^{-2}$ .

The performance of several versions of Affine Space estimators under the same test conditions

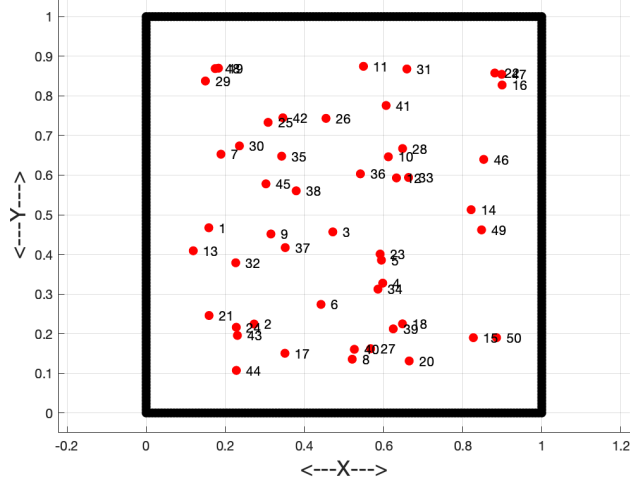


Figure 20: An illustration of 50 random sensors.

has been reported in [5]. The computationally most expensive but also most accurate Optimal Affine Space estimator achieves in this experiment roughly an  $H^1$ -error of size  $3 \times 10^{-3}$  which is slightly better than the accuracy  $8 \times 10^{-3}$ , observed for eRNN. However, when lifting the cap of at most 10,000 training steps, the observed maximal  $H^1$ -error for eRNN drops also to  $5 \times 10^{-3}$  in the 50-sensor case, which is at the same level as what the best affine estimator achieves. In summary, it seems that for this type of problems both types of estimators achieve about the same level of estimation accuracy and nonlinearity of the neural network lifting map does not seem to offer substantial advantages for scenario (S1). There is instead a noteworthy difference regarding computational cost in relation to predictable training success. The above example shows that neural networks may have significant disadvantages with regard to optimization success and incurred computational cost in comparison with affine-space recovery schemes where, however, eRNN shows a consistent level of reliability that avoids degrading accuracy under over-parametrization.

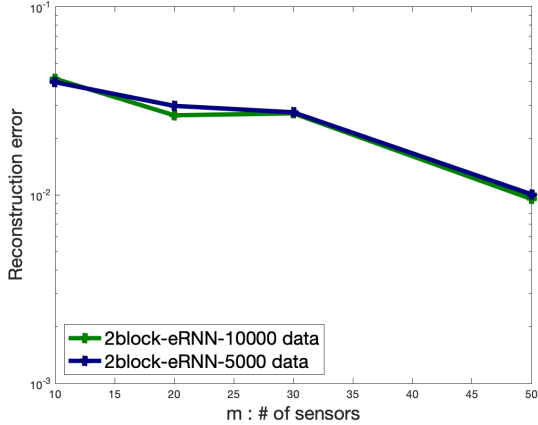


Figure 21: Predicted with eRNN

Figure 22: Max reconstruction  $H^1$  errors among 1000 testing samples with eRNN.

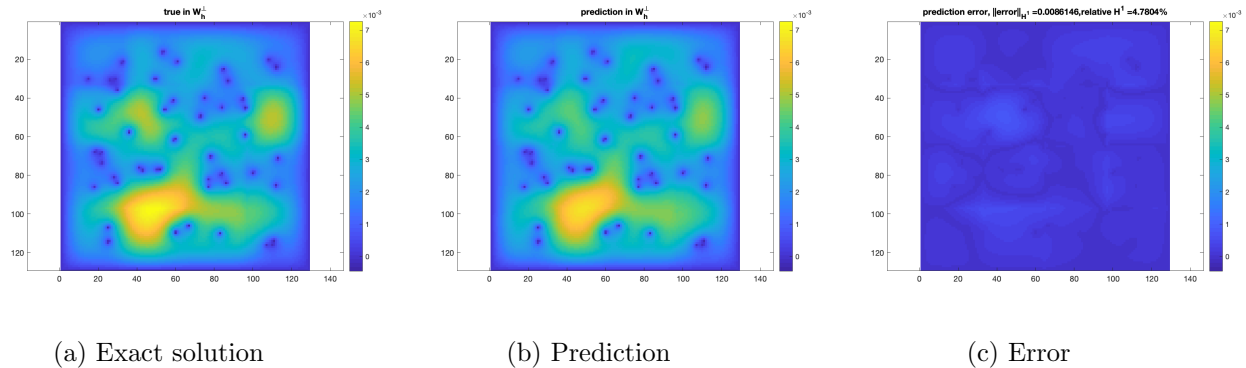


Figure 23: An example of exact vs. eRNN predicted solution in  $W_h^T$  for 50 random sensors case.

## 7 Summary

Overall, the experiments for the two application scenarios (S1), (S2) reflect the following general picture. Regardless of a specific training mode accuracy improves rapidly at the beginning and essentially saturates at a moderate network complexity. Beyond that point further improvements require a relatively substantial training effort which may not even be rewarded in the RNN mode. Instead, eRNN usually responds with slight improvements and essentially never with an accuracy degradation. While in a number of cases eRNN achieves a smaller generalization error than plain RNN, by and large, the differences in accuracy are not overly significant. Once the generalization error curve starts flattening, additional increases of network complexity seem to just increase over-parametrization and widen a flat plateau fluctuating around “achievable” local minima. Instead a realization of theoretically possible expressive power seems to remain highly improbable. Aside from an increased robustness with respect to algorithmic settings, the main advantage of eRNN

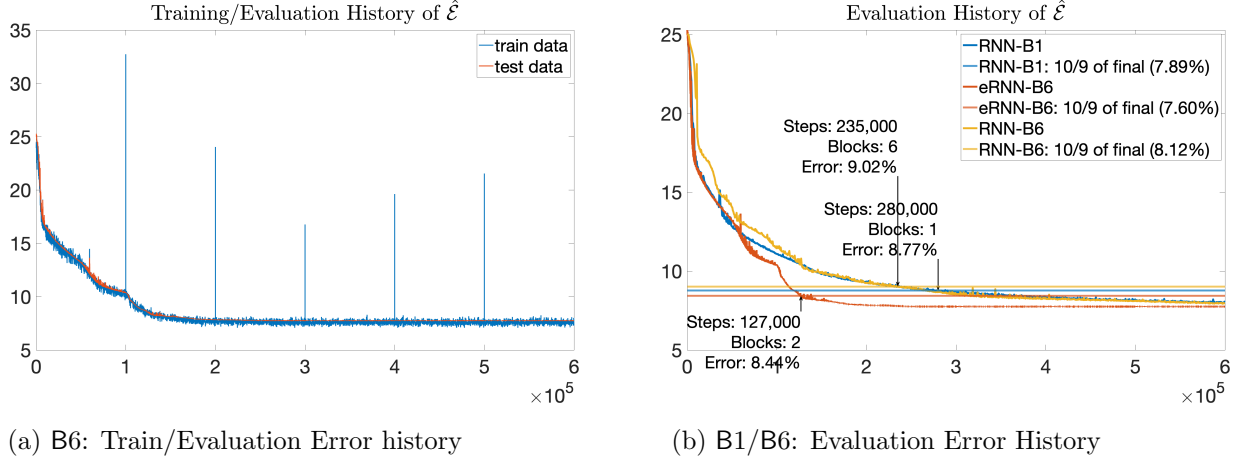


Figure 24: Train-log-normal-sen16-POD-L<sub>2</sub>, W20-O21-Ir0.02

over RNN seems to lie in substantial savings of computational work needed to nearly realize an apparently achievable generalization accuracy. This is illustrated by Figure 24, (b), recording the work needed to achieve 10/9 of the smallest generalization error achieved by the respective training modality. It is also interesting to note that the generalization errors at various optimization stages are not much larger than the corresponding relative loss-size, reflecting reliability of the schemes, see Figure 24, (a).

## References

- [1] P. Binev, A. Cohen, W. Dahmen, R. DeVore, G. Petrova, and P. Wojtaszczyk, *Convergence Rates for Greedy Algorithms in Reduced Basis Methods*, SIAM Journal of Mathematical Analysis **43**, 1457-1472, 2011.
- [2] P. Binev, A. Cohen, W. Dahmen, R. DeVore, G. Petrova, and P. Wojtaszczyk, *Data assimilation in reduced modeling*, SIAM/ASA J. Uncertain. Quantif. **5**, 1-29, 2017.
- [3] A. Cohen and R. DeVore, *Approximation of high dimensional parametric pdes*, Acta Numerica, 2015.
- [4] A. Cohen, W. Dahmen, R. DeVore, J. Fadili, O. Mula and J. Nichols, *Optimal reduced model algorithms for data-based state estimation*, submitted to SIAM Journal of Numerical Analysis, 2020.
- [5] A. Cohen, W. Dahmen, R. DeVore, J. Nichols, Reduced Basis Greedy Selection Using Random Training Sets, ESAIM: M2AN, 54 (no 5) (2020), 1509–1524, <https://doi.org/10.1051/m2an/2020004>, doi: 10.1051/m2an/2020004, <http://arxiv.org/abs/1810.09344> [math.NA].

- [6] A. Cohen, W. Dahmen, O. Mula, J. Nichols, Nonlinear reduced models for state and parameter estimation, <https://arxiv.org/submit/3356244>
- [7] W. Dahmen, C. Plesken, G. Welper, *Double Greedy Algorithms: Reduced Basis Methods for Transport Dominated Problems*, ESAIM: Mathematical Modelling and Numerical Analysis, 48(3) (2014), 623–663. DOI 10.1051/m2an/2013103, <http://arxiv.org/abs/1302.5072>.
- [8] W. Dahmen, R. Stevenson, J. Westerdiep, Accuracy controlled data assimilation for parabolic problems, preprint, Oct. 2020, <https://arxiv.org/abs/2105.05836>, to appear in Math. Comp.
- [9] N. Dal Santo, S. Deparis, L. Pegolotti, Data driven approximation of parametrized PDEs by Reduced Basis and Neural Networks, 2019, arXiv:1904.01514v1 [cs.NA].
- [10] Y. Maday, A.T. Patera, J.D. Penn and M. Yano, *A parametrized-background data-weak approach to variational data assimilation: Formulation, analysis, and application to acoustics*, Int. J. Numer. Meth. Eng. **102**, 933-965, 2015.
- [11] G. Rozza, D.B.P. Huynh, and A.T. Patera, *Reduced basis approximation and a posteriori error estimation for affinely parametrized elliptic coercive partial differential equations - application to transport and continuum mechanics*, Archive of Computational Methods in Engineering **15**, 229-275, 2008.
- [12] D. Braess, Finite Elements, Theory, Fast Solvers, and Applications in Solid Mechanics, Cambridge University Press, 1997.
- [13] K. Bhattacharya, B. Hosseini, N.B. Kovachki and A.M. Stuart, *Model reduction and Neural Networks for parametric PDEs*, Arxiv Preprint: <https://arxiv.org/pdf/2005.03180.pdf>
- [14] D.P. Kroese and Z.I. Botev, *Spatial process simulation* in Stochastic geometry, spatial statistics and random fields, Springer, 369-404, 2015.
- [15] C.R. Dietrich and G.N. Newsam, *Fast and exact simulation of stationary Gaussian processes through circulant embedding of the covariance matrix*, SIAM Journal on Scientific Computing, 18(4), 1088-1107, 1997.